

# On the Stability of Oscillatory Modes in an Oscillator Based on a Distributed Amplifier

Jan Filip<sup>1</sup>, Graduate Student Member, IEEE, Almudena Suárez<sup>2</sup>, Fellow, IEEE,  
and Zbyněk Škvor<sup>1</sup>, Senior Member, IEEE

**Abstract**—An in-depth investigation of oscillation modes in an oscillator based on a distributed amplifier is presented. It shows that instability problems reported in previous papers are intrinsic to the circuit nonlinear dynamics. The undesired phenomena include discontinuous jumps when continuously varying the tuning voltage, quasi-periodicity, or two incommensurable self-generated oscillations, and nonuniqueness of the mode, meaning that the same frequency can be achieved by several combinations of tuning voltages. The numerical bifurcation analysis of the circuit reveals a complicated dynamical structure that explains the mechanisms leading to the reported undesired behaviors. Special attention is paid to the presence of complicated bifurcation scenarios leading to quasi-periodic behavior and a chaotic regime. The results of this theoretical investigation are confirmed by independent numerical simulations through time-domain integration and qualitatively predict the experimental observations. Then, a stabilization procedure based on the introduction of resistors is presented, evaluating its impact on the oscillation amplitude and the uniqueness of the desired oscillation modes obtained when tuning the bias voltages.

**Index Terms**—Delay line oscillator, invariant manifold, local bifurcation, Neimark–Sacker bifurcation.

## I. INTRODUCTION

THE concept of an oscillator based on a distributed amplifier was first introduced in [1] and later experimentally verified in [2] and [3]. The ability of a distributed amplifier to overcome the fundamental Bode–Fano limit is well recognized [4], and the distributed-amplifier oscillator should take advantage of the extreme bandwidths that the distributed amplifier can reach. To illustrate its operation mechanism, Fig. 1 presents the schematics of the three-stage microstrip distributed amplifier oscillator that will be considered here. Transistors are connected to the shared transmission line (TL) with equidistant spacing  $l$  forming a multiple delay line feedback path. For clarity, feedback loops for each transistor (conceptually represented with the transfer functions  $H_i$ )

Manuscript received 25 August 2022; revised 29 October 2022; accepted 25 November 2022. This work was supported in part by the Czech Technical University in Prague (CTU) Project under Grant SGS22/162/OHK3/3T/13 and in part by the Spanish Ministry of Science and Innovation (MCIN/AEI/10.13039/501100011033) under Grant PID2020-116569RB-C31. (Corresponding author: Jan Filip.)

Jan Filip and Zbyněk Škvor are with the Department of Electromagnetic Field, Czech Technical University in Prague, 166 27 Prague, Czech Republic (e-mail: filipj17@fel.cvut.cz).

Almudena Suárez is with the Departamento de Ingeniería de Comunicaciones, Universidad de Cantabria, 39005 Santander, Spain.

Color versions of one or more figures in this article are available at <https://doi.org/10.1109/TMTT.2022.3226454>.

Digital Object Identifier 10.1109/TMTT.2022.3226454

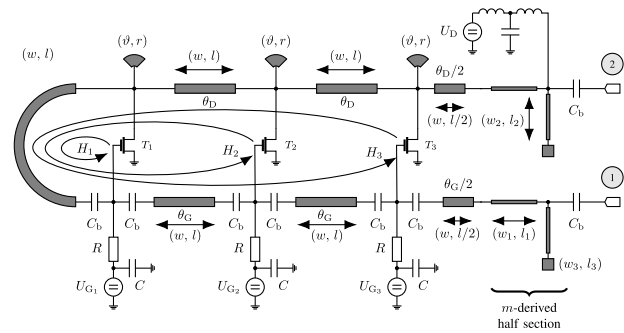


Fig. 1. Microstrip realization of the distributed-amplifier oscillator.

are indicated with arrows. The microstrip TL of width  $w$  is periodically loaded by the parasitic capacitances of the active devices with equidistant spacing  $l$ . To ensure small reflections in an as-wide-as-possible bandwidth of the distributed amplifier, the structure is conventionally terminated by Zobel's  $m$ -derived half sections [5] providing an optimal wideband match to the real load  $R$  purely with the parameter value  $m \doteq 0.6$  [4], [6]. According to Floquet's theorem, a slow Bloch wave can be excited in such a structure [7]. The operation regime of the distributed amplifier oscillator is intended for the first passband given by the Bragg condition [7].

The frequency tuning control mechanism of the distributed amplifier oscillator relies on the variation of the transconductances of adjacent pairs of active elements. This is done most conveniently by adjusting the gate bias voltage of each stage. The tuning, as interpreted in previous works [2], [8], gives rise to a vector addition of the waves propagating from the active elements in the common part of the artificial line. The tuning function is then constructed by solving the system for the amplitude and phase terms in two unknown transconductances, such that the Barkhausen condition is fulfilled [2]. Indeed, it was experimentally observed [2], [3], [8], [9] that, by a careful adjustment of the bias voltages of adjacent transistors pairs, it is possible to cover all frequencies from  $0.31\omega_c$  up to  $\omega_c$  ( $\omega_c$  is the cutoff frequency of the artificial TL). However during the process of tuning, quasi-periodic oscillations, hysteresis, and jumps to undesired modes occur, as reported in several previous works [2], [3], [9]. In addition, some oscillation modes are experimentally observed when varying the tuning voltages in a certain sense only. This is an indication of the complex underlying dynamics that will extremely complicate the task of achieving an optimal tuning function. To date, it is not clear if the undesired phenomena have their origin in an

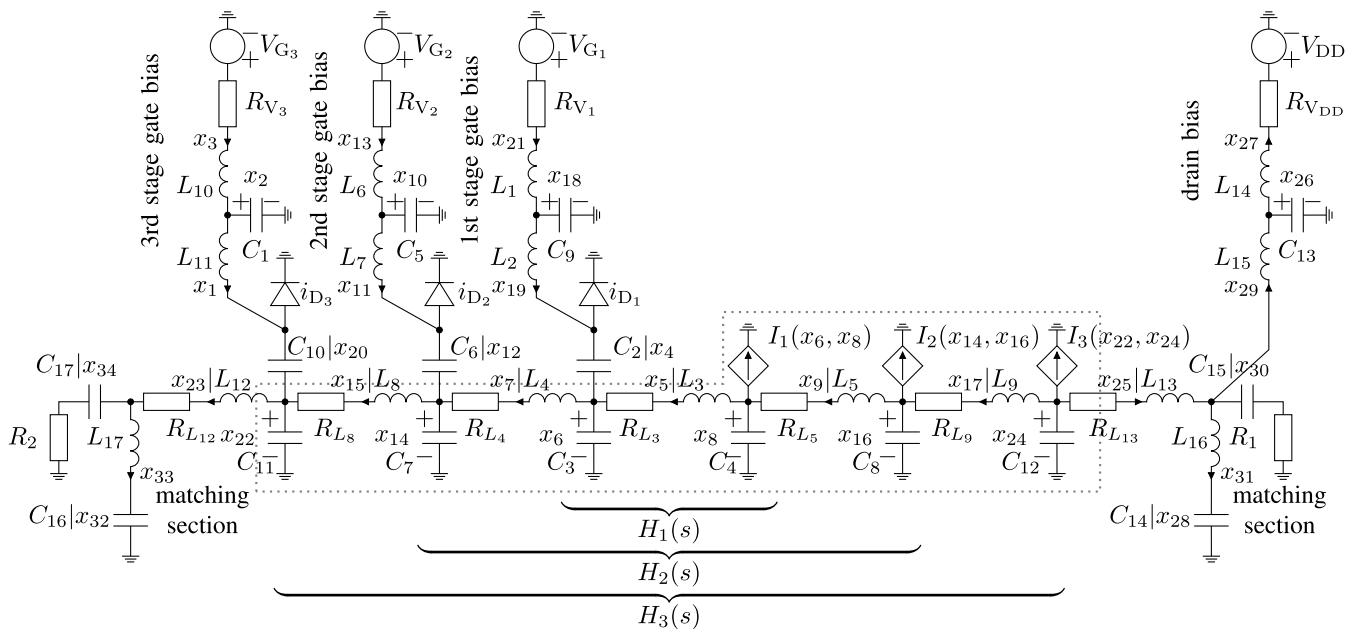


Fig. 2. Three-stage distributed amplifier oscillator under investigation.

imperfect circuit implementation or if they are inherent to the circuit dynamics.

Previous works on the distributed amplifier oscillator [3], [8] base the oscillatory modes prediction on the Barkhausen criterion. Even though this small-signal prediction may partially agree with the measurement, the mechanism for the oscillation buildup is somewhat more complicated due to the multiresonant nature of the involved feedback loops (Fig. 1). The studies [8], [9] present a harmonic balance analysis of the oscillatory solutions, complemented with a stability analysis based on the envelope transient method that uses these solutions as an initial value. Unfortunately, the envelope-transient is not rigorous enough for the prediction of the stability properties due to its dependence on the integration time step [10]. In fact, the analysis and design of distributed oscillators miss a detailed and rigorous mathematical investigation of the instability mechanisms that often plague the practical implementations. This investigation is the main contribution of our work.

To address the origin of the undesired phenomena, here, we propose a simplified yet realistic model of the oscillator that is independent of implementation nuances. One of the goals is to demonstrate, for a canonical circuit representation, that mode jumps are not caused by parasitic effects. Thus, their occurrence will be independent of the implementation. A second fundamental goal is to verify that the desired oscillations can be reliably achieved as stable and unique solutions. Initially, we will perform a small-signal analysis in the complex-frequency domain, which will provide insight into the mechanisms for the generation of the oscillation modes. This will be achieved through the calculation of the circuit characteristic determinant [11]. As will be shown, only some of the detected modes are intended in the design. Then, we will carry out a detailed bifurcation analysis that will be used as a general framework for a qualitative description of the complex nonlinear dynamics of the circuit. Hopf bifurcations

can lead to stable oscillations, so knowing their trajectories in the plane defined by the two control voltages will reveal how the oscillations appear during the oscillator tuning. Special attention is paid to the presence of complicated bifurcation scenarios leading to quasi-periodic behavior and a chaotic regime.

The results of this theoretical investigation will be confirmed by independent numerical simulations through time-domain integration and selected experimental measurements. As will be shown, the theoretical analysis qualitatively predicts the experimental observations. A stabilization mechanism through the introduction of resistors will also be presented, considering its impact on the oscillator performance.

In addition to the nonlinear-dynamics investigation, the manuscript provides practical methods for stability analysis and bifurcation detection, compatible with commercial simulators, and a full description of the circuit with arbitrary models and parasitic effects. Those practical methods rely on the calculation of the total admittance matrix of the complete oscillator topology, defined at the device terminals.

This article is organized as follows. Section II describes the small-signal analysis of the distributed amplifier oscillator, and the results are compared with those in previous works [1], [2]. Section III presents a novel nonlinear state-space model of the three-stage oscillator and outlines the stability analysis strategy utilizing bifurcation theory. In Section IV, a detailed stability analysis of each oscillator stage is provided. Section V is devoted to the Hopf loci computation, which is closely related to the actual tuning of the oscillator. Finally, Section VI describes the possible stabilization of the oscillator.

## II. SMALL-SIGNAL STABILITY ANALYSIS

The study [1] proposed an oscillator based on the introduction of a feedback path in a distributed amplifier, as shown in Fig. 1, which can be described with the simplified equivalent circuit of Fig. 2. The distributed-amplifier oscillator is intended

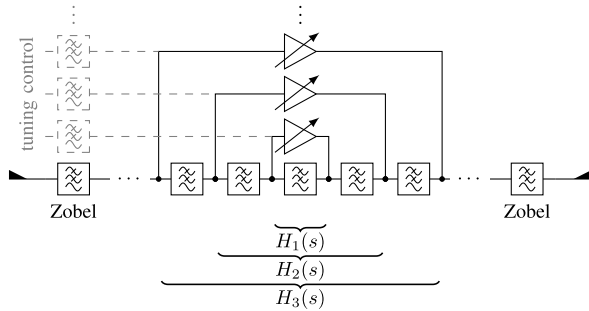


Fig. 3. Conceptual schematic of the distributed-amplifier oscillator.

to be a wideband voltage-controlled oscillator (VCO) tuned by gate voltage pairs by biasing adjacent active devices. The conceptual schematic of Fig. 3 illustrates the entire idea of the tuning mechanism. The active devices are inside multiresonant feedback paths, and when using simple gain models for the active devices, these paths can be represented as feedback operators  $H_i(s)$ ,  $s \in \mathbb{C}$ . All the operators  $H_i(s)$  are rational functions with the same cutoff frequency  $\omega_c$ , but the number of poles gradually grows with  $i = 1, 2, 3, \dots$ . This multiresonant nature of the feedback structure is the reason for the unreliable behavior that will be investigated here. Changes in the gains of the active devices lead to various oscillation frequencies, because the oscillation buildup condition is determined by the simultaneous action of the involved active devices of nonzero gain. In fact, for the calculation of the possible oscillation frequencies, in [2] and [3], it was initially assumed that only the  $i$ th device was active. When using a feedback line consisting of a particular phaselength [1], and provided that the open loop gain is greater than unity, oscillation can occur at the frequencies

$$\Omega_n^{(i,k)} = \sin\left(\frac{\pi(2k-1)}{4i-2}\right), \quad k = 1, 2, \dots \quad (1)$$

where  $\Omega_n$  is the frequency normalized to cutoff frequency  $\omega_c$  of the line. At each  $k$ , the closed-loop phase shift is  $k2\pi$ . In [3], it was argued that the oscillation always occurs at the frequency corresponding to  $k = 1$ . Thus, the desired oscillations will be of the kind  $\Omega_n^{(i,1)}$ . A practical problem is that oscillations can also arise for  $k > 1$ , thus, corresponding to modes  $\Omega_n^{(i,k)}$ , where  $k > 1$ , as will be shown in this work.

In fact, the desired tuning range of the oscillator is between  $\Omega_n^{(2,1)}$  and  $\Omega_n^{(1,1)}$ , and between  $\Omega_n^{(3,1)}$  and  $\Omega_n^{(2,1)}$  [1], [2], [3]. Thus, careful tuning of the adjacent sections in the three-stage oscillator has to cover a considerable range of frequencies from  $\Omega_n^{(3,1)} \doteq 0.31$  to  $\Omega_c = 1$ . Remember that frequencies are normalized to the cutoff frequency  $\omega_c = 2/\sqrt{LC}$  of the artificial TL.

In this section, a small-signal stability analysis of the distributed-amplifier oscillator will be carried out, based on the calculation of the characteristic determinant, and the results will be compared with those obtained in previous works [1], [2], [3]. The active devices in Fig. 2 will be considered as linear voltage-controlled current sources with the transconductances  $g_{m_i}$ . Note that in Section IV, a more

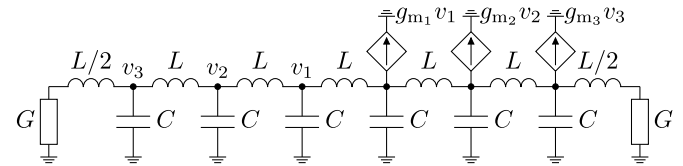


Fig. 4. Simplified small-signal equivalent of the full circuit.

realistic nonlinear description of these active devices will be introduced, using voltage-controlled nonlinear current sources.

For simplicity, normalized values  $R = 1$  and  $C = L = 2$  will be assumed, since this normalization does not affect the results. Hence, the artificial TL will have the cutoff frequency  $\omega_c = 2/\sqrt{LC} = 1$  and the characteristic impedance  $Z = 1$ . Note that this is a fundamental, general representation of the distributed-amplifier oscillator, as this topology was proposed in [1].

For the stability analysis, we will consider a small-amplitude perturbation of complex frequency  $s = \Sigma + j\Omega$ . Then, we will obtain the total admittance matrix at the perturbation frequency  $s$ , considering the reduced small-signal equivalent (see Fig. 4) LC-ladder structure inside the dotted area of the structure in Fig. 2. Both ends of the artificial TL in the small-signal model are considered to be terminated by the conductance  $G = 1/Z$ , as shown in Fig. 4. As stated, general current sources  $I_i$  at a given bias point are modeled as linear voltage-controlled current sources of a given transconductance  $g_{m_i}v_i \cong I_i$ ,  $i = 1, 2, 3$ . Such a structure has an admittance matrix  $\mathbf{Y}(s)$  (see (2), shown at the bottom of the next page). The circuit natural frequencies are given by the zeroes of the matrix determinant, which agrees with the system characteristic determinant.

In Fig. 5(a), we present the variation of the natural frequencies in the upper complex plane (root loci) when sweeping the transconductances of the first and second stages, that is, the variation of the roots of  $\det \mathbf{Y}(s, g_{m_1}, g_{m_2})$ . In Fig. 5(a), as the color changes to yellow, the normalized transconductance of the first stage [Fig. 5(a)] is varied from 0 to 4. In Fig. 5(b), the same variation is considered for the transconductance of the second stage. The sense of variation of the natural frequencies, when increasing  $g_{m_1}$  and  $g_{m_2}$ , is indicated with arrows. Black diamond marks show the original positions of the natural frequencies when all the transconductances are zero. There is one pair of complex conjugate natural frequencies close to the imaginary axis at about  $\Omega_c = 1$  corresponding to the undesired mode  $\Omega_n^{(2,2)}$ . The actual position of the poles deviates a little from  $\Omega_c$ . This is due to the fact that in the simplified model, we do not consider the matching  $m$ -derived half section used in [3]. For any nonzero transconductance value, it rapidly shifts to the right-hand side (RHS). In fact, for each crossing of a pair of complex-conjugate frequencies to the RHS, a Hopf bifurcation occurs, at which point a periodic oscillatory solution is generated from zero steady-state amplitude. There are Hopf bifurcations giving rise to oscillations at the undesired mode  $\Omega_n^{(2,2)}$  and at the desired mode  $\Omega_n^{(2,1)}$ . The occurrence of a particular Hopf bifurcation does not mean that the generated periodic steady-state solution will be stable; in fact, a periodic solution generated from an unstable

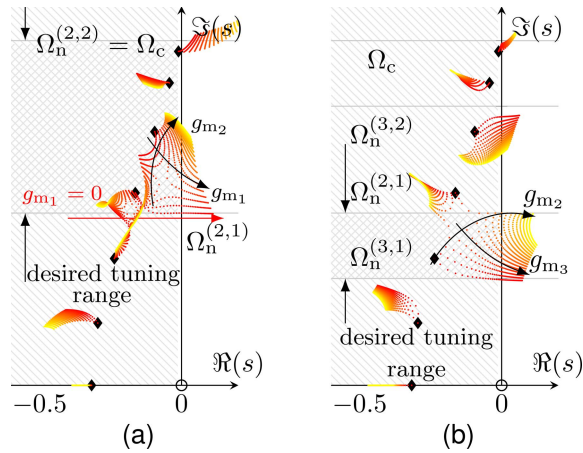


Fig. 5. Trajectories of the zeroes of  $\det \mathbf{Y}(s, g_{m_i}, g_{m_{i+1}})$ , or circuit natural frequencies, in the complex plane  $\Sigma + j\Omega$ . (a) First and second active stages (i.e.,  $i = 1$ ). (b) Second and third active stages (i.e.,  $i = 2$ ). Transconductances were varied in the  $[0; 4]$  range. In (a) and (b), natural frequencies are crossing the imaginary axis in multiple regions.

dc solution will be unstable, at least in the neighborhood of the bifurcation, as established by the bifurcation relationships [12]. Even if unstable near the bifurcation, a periodic solution may stabilize, as the parameter is further varied, which can only be predicted through a stability analysis of the steady-state oscillation. On the other hand, in the presence of two or more pairs of complex conjugate natural frequencies in the RHS, the physical solution may be quasi-periodic or even chaotic. As an example, let us consider loci in Fig. 5(a). When only the second stage of the oscillator is active (nonzero transconductance  $g_{m_2}$ ) and increasing  $g_{m_2}$ , we observe the crossing of a pair of complex-conjugate frequencies near  $\Omega_n^{(2,2)} = \Omega_c = 1$  (undesired mode). Then, for a larger  $g_{m_2}$ , we have the crossing of a second pair at  $\Omega_n^{(2,1)} = 1/2$  (desired mode)—see the red arrow. The mode at  $\Omega_n^{(2,2)} = \Omega_c = 1$  occurs first, so the desired one is initially unstable. However, this mode may stabilize under a further variation of the tuning parameter. However, this mode may stabilize under a further variation of the tuning parameter. As stated, the prediction of

this stabilization requires a stability analysis of the steady-state oscillation. This complicated behavior is investigated in Section IV.

In Fig. 5(b), we present the variation of the natural frequencies when sweeping the transconductances of the second and third stages. The expected tuning range is between the first modes ( $k = 1$ ) of their respective frequencies  $\Omega_n^{(3,1)}$  and  $\Omega_n^{(2,1)}$ . As seen in Fig. 5(b), there also exist undesired crossings of the imaginary axis at a frequency slightly below that of the undesired mode  $\Omega_n^{(3,2)}$  of the third stage and in the neighborhood of the mode  $\Omega_n^{(3,3)} = \Omega_c$ .

Clearly, in the two cases considered in Fig. 5, there exist tuning-parameter combinations for which a considerable interval of the imaginary axis  $j\Omega$  is crossed with  $k = 1$ . However, in view of the additional crossings with  $k > 1$  and taking into account the bifurcation relationships [12], there is no guarantee that the physical oscillation will occur for  $k = 1$  as Divina and Škvor [2], [3] had stated. In Section IV, we will address the steady-state analysis of the generated periodic modes. As shown in Section IV, the Hopf bifurcations predicted with the characteristic determinant are fully consistent with the results of this analysis, based on time-domain continuation.

### III. DERIVATION OF THE STATE-FORM SYSTEM

In this section, the circuit in Fig. 2 will be conveniently modeled and formulated to enable its nonlinear analysis with a well developed toolkit of bifurcation theory [13], [14], [15]. Such a toolkit requires the smoothness of all the considered functions, as well as a representation of the system in state form. As a result, one should avoid differential-algebraic equations, even though these can be more easily obtained using modified nodal analysis, and obtain a proper state-space form formulation [16]. This is, in fact, a difficult and laborious task. There are works that deal with simple circuits with one or two bipolar junction transistors (BJTs) [17], but, due to the considerable complexity of the problem, circuit models with multiple active devices and a large number of reactances do not appear in the literature. To the best of our knowledge,

$$\mathbf{Y}(s) = \begin{bmatrix} G + \frac{2}{sL} & -\frac{2}{sL} & 0 & 0 & 0 & 0 & 0 & 0 & 0 \\ -\frac{2}{sL} & sC + \frac{3}{sL} & -\frac{1}{sL} & 0 & 0 & 0 & g_{m_3} & 0 & 0 \\ 0 & -\frac{1}{sL} & sC + \frac{2}{sL} & -\frac{1}{sL} & 0 & g_{m_2} & 0 & 0 & 0 \\ 0 & 0 & -\frac{1}{sL} & sC + \frac{2}{sL} & g_{m_1} - \frac{1}{sL} & 0 & 0 & 0 & 0 \\ 0 & 0 & 0 & -\frac{1}{sL} & sC + \frac{2}{sL} & -\frac{1}{sL} & 0 & 0 & 0 \\ 0 & 0 & 0 & 0 & -\frac{1}{sL} & sC + \frac{2}{sL} & -\frac{1}{sL} & 0 & 0 \\ 0 & 0 & 0 & 0 & 0 & -\frac{1}{sL} & sC + \frac{3}{sL} & -\frac{2}{sL} & 0 \\ 0 & 0 & 0 & 0 & 0 & 0 & -\frac{2}{sL} & G + \frac{2}{sL} & 0 \end{bmatrix} \quad (2)$$

here, we will present the first detailed bifurcation analysis of a multidevice oscillator, performed through a time-domain continuation.

In order to formulate the system with the first derivative of physical quantities only, and because there is no proper voltage tree and current co-tree in the circuit [16], the state variables considered are the inductor currents  $i_L(t)$ , the voltages across the capacitors  $v_C(t)$ , and the capacitor charges  $q_C(t)$ . As in Section II, we will limit the number of stages to  $N = 3$ . The resulting autonomous system of ordinary differential equations (ODEs) is shown in the Appendix. This system can be written compactly in the form

$$\dot{\mathbf{x}}(t) = \mathbf{A}(\mu)\mathbf{x}(t) + f(\mathbf{x}(t), \mu) \quad (3)$$

where  $t \in \mathbb{R}$  stands for time,  $\mathbf{x} \in \mathbb{R}^n$  represents the vector of state variables,  $\mathbf{A} \in \mathbb{R}^{n \times n}$  describes the circuit linear part, the smooth arbitrary function  $f$  models both passive and active nonlinearities, and  $\mu \in \mathbb{R}^m$  is the parameter vector including the bias voltages.

The requirement for smoothness of the system equations is crucial; otherwise, the dimensionality of the switching manifold, when a problem is formulated as a piecewise-smooth system (Filippov systems), is unbearably high [18], [19]. Therefore, instead of piecewise-smooth FET modeling, we use a properly scaled smooth approximation of the Heaviside step function belonging to the logistic-function family, applied to the hybrid modification of Sussman-Fort et al. [20], Curtice [21], [22], and Statz et al. [23] GaAs MESFET model. The active devices are modeled as nonlinear voltage-dependent current sources given by

$$i(x, y) = \frac{e^{2\sigma(x-V_T)}}{e^{2\sigma(x-V_T)} + 1} \beta(x - V_T)^2 (1 + \lambda y) \tanh \gamma y \quad (4)$$

where we use<sup>1</sup> steepness coefficient  $\sigma = 10^4$ , pinch-off voltage  $V_T = -1$  V, saturation voltage parameter  $\gamma = 2$  V<sup>-1</sup>, channel length modulation parameter  $\lambda = 0$ , and transconductance parameter  $\beta = 0.08$  AV<sup>-2</sup>. First argument  $x$  is used for gate-source voltage, and second argument  $y$  for the drain voltage. Time scaling is introduced for the numerical stability of continuation algorithms with the parameters given in the Appendix. Time scaling for the dynamic part is as follows:

$$L \frac{di}{dt} = kL \frac{di}{d(kt)} \quad (5)$$

$$C \frac{dv}{dt} = kC \frac{dv}{d(kt)}. \quad (6)$$

This way both the reactive elements and the time variable are scaled, which will result into a new cutoff frequency of the artificial TL  $\omega_{\text{scaled}} = k\omega_{\text{original}}$ . Value  $k$  has to be chosen as a trade-off between large values in bias circuits and much smaller values in the RF part of the circuit to obtain a satisfying numerical convergence of the continuation algorithm that does not affect the qualitative properties of the oscillator.

<sup>1</sup>These values were considered in order to follow the values of the obsolete original 2–18-GHz low noise pseudomorphic high-electron-mobility-transistor (pHEMT) ATF35376 (Hewlett-Packard) used in [2] and [3].

Divina and Škvor's [2] element choice was:  $L = 125$  nH and  $C = 50$  pF, which produces  $Z = 50$   $\Omega$  and  $f_c = \omega_c/2\pi \doteq 127$  MHz. In our work, we scaled<sup>2</sup> the dynamical part of the circuit with  $k = 1 \cdot 10^6$ , which gives us  $f_c = \omega_c/2\pi \doteq 127$  Hz, while  $Z = 50$  is not affected. As a result, the parameters of the nonlinear transistor model do not have to be modified.

Also note that diodes modeling depleted layer effects at the transistor gates in the schematics in Fig. 2 are not critical in the presented analysis and can be omitted. The study is, thus, not encumbered by parasitic influences; instead, we will investigate the essential dynamical properties inherent to the circuit.

The stability analysis and construction of the tuning function for the distributed amplifier oscillator are addressed by finding the solution paths of (3) through a time-domain continuation, instead of using either conventional time-consuming integration or harmonic balance. In the following, we describe the theoretical foundations of time-domain continuation and stability analysis.

#### A. Periodic Solution Curves

The solution curves will be computed numerically utilizing predictor-corrector methods also known as continuation. This performed using the Moore-Penrose continuation algorithm [24], [25] implemented in CL\_MATCONT routines. Singularities are detected using specially designed test functions; see, for example, [13].

We will consider the RHS of (3) as a state space flow  $\mathbf{A}(\mu)\mathbf{x}(t) + f(\mathbf{x}(t), \mu) := \Phi(\mathbf{x}, \mu, t)$  parametrized both by  $\mu$  and  $t$ . The periodic solutions (or limit cycles) are computed as a boundary value problem [26]

$$\dot{\mathbf{x}}(t) - T\Phi(\mathbf{x}(t), \mu) = 0 \quad (7)$$

$$\mathbf{x}(0) - \mathbf{x}(1) = 0 \quad (8)$$

$$\int_0^1 \dot{\mathbf{x}}(t)^T \mathbf{x}(t) dt = 0 \quad (9)$$

using an orthogonal collocation method on the normalized interval  $t \in [0; 1]$ , treating period  $T$  as a free parameter. The second equation imposes the  $T$  periodicity of the solution. However, due to the autonomy of the circuit, such solutions are invariant under a translation of phase; hence, the last of the equations makes the entire boundary value problem system unique by fixing the phase where  $\dot{\mathbf{x}}(t)$  is the derivative of the previous solution. For implementation details of the numerical continuation and singularity detection, see [26].

#### B. Stability Analysis

To make the manuscript self-contained, the key concepts to be used in the analysis of Section IV will be briefly

<sup>2</sup>Note that the *scaling* should not be confused with *normalization* used throughout this article with capitalized letters: for instance,  $\Omega$  is just  $\Omega = \omega_{\text{scaled}}/\omega_{\text{scaled}}$ . In order to obtain the absolute values of frequency, the reader needs to multiply the frequency  $\Omega$  by  $\omega_{\text{scaled}}$  or simply by 127 Hz. The use of normalized results is much more clear in the view of the notation for discrete modes  $\Omega_n^{(i,k)}$  introduced in Section II.

summarized here. An invariant set  $S$  of (3) is a set of points  $\mathbf{x} \in S$  that is invariant under the flow  $\Phi$  [13], i.e.,

$$\mathbf{x} \in S \implies \Phi(\mathbf{x}, \mu, t) \in S \quad \forall t \in \mathbb{R}. \quad (10)$$

If  $\mathbf{x}_0 \in S$  is the only element of the invariant set  $S$ , we will call it an equilibrium point (EP) or dc solution, which will fulfill

$$\mathbf{0} = \Phi(\mathbf{x}, \mu, t). \quad (11)$$

To determine the stability properties of  $\mathbf{x}_0$ , the Jacobian matrix  $D\Phi(\mathbf{x}_0, \mu, t) := D\Phi(\mu)|_{\mathbf{x}_0}$  must be obtained. The EP  $\mathbf{x}_0(\mu)$  is stable if all the eigenvalues  $\lambda_i$  associated with the linearization  $D\Phi(\mu)|_{\mathbf{x}_0}$  have a negative real part [14], i.e.,  $\text{Re } \lambda_i < 0, \forall i, i = 1, 2, \dots, n$ . Note that these eigenvalues agree with the roots of the characteristic determinant analyzed in Section II.

The second invariant set of interest in oscillator design is obtained when  $T \in \mathbb{R}^+$ , such that

$$\Phi(\mathbf{x}, \mu, t + T) = \Phi(\mathbf{x}, \mu, t) \quad (12)$$

and  $S$  is called a periodic orbit. Moreover, if  $T_0$  is the smallest  $T$  in (12) and there is no other periodic orbit in the neighborhood of  $S$ ,  $S$  is called a  $T_0$ -periodic limit cycle and is denoted as  $\Gamma(\mu)$  [14], [15]. The fundamental solutions of the system (3) are given by the  $T$ -periodic time-varying matrix  $\mathbf{M}(t)$  satisfying

$$\dot{\mathbf{M}}(t) = D\mathbf{M}(t) \quad (13)$$

with the initial condition  $\mathbf{M}(0) = \mathbf{I}$ , where  $\mathbf{I} \in \mathbb{R}^{n \times n}$  is the identity matrix, and  $D$  is the Jacobi operator as used previously. We call  $\mathbf{M}(T)$  the monodromy matrix [13]. The eigenvalues of  $\mathbf{M}(T)$

$$1, \mu_1, \dots, \mu_{n-1} \quad (14)$$

are called the Floquet multipliers of the periodic orbit [13], [14]. The stability properties of periodic solutions are formulated in terms of a unit disk where the boundary plays the same role as the imaginary axis for the dc solutions in Section II. If any Floquet multiplier fulfills  $|\mu_k| > 1$ ,  $k = 1, \dots, n - 1$ , the limit cycle is said to be unstable. Note that in any free-running oscillator, there is a trivial Floquet multiplier  $|\mu_0| = 1$  associated with the phase invariance; see (7). There are three main types of local bifurcation [14]: fold or turning point, when a real multiplier crosses the unit circle through  $(1, 0)$ , period doubling, when a real multiplier crosses the unit circle through  $(-1, 0)$ , and Neimark–Sacker, when a pair of complex conjugate multipliers cross the unit circle through  $1e^{\pm j\Phi_0}$ ,  $0 < \Phi_0 < \pi$ , which leads to a quasi-periodic regime.

#### IV. STABILITY ANALYSIS VERSUS TUNING VOLTAGES

In this section, we will present a stability analysis of the distributed oscillator versus the tuning voltage of each of the three active devices when the other two devices are off. Note that this is the same situation considered in the prediction of the oscillation frequencies carried out in [1], and resulting in expression (1).

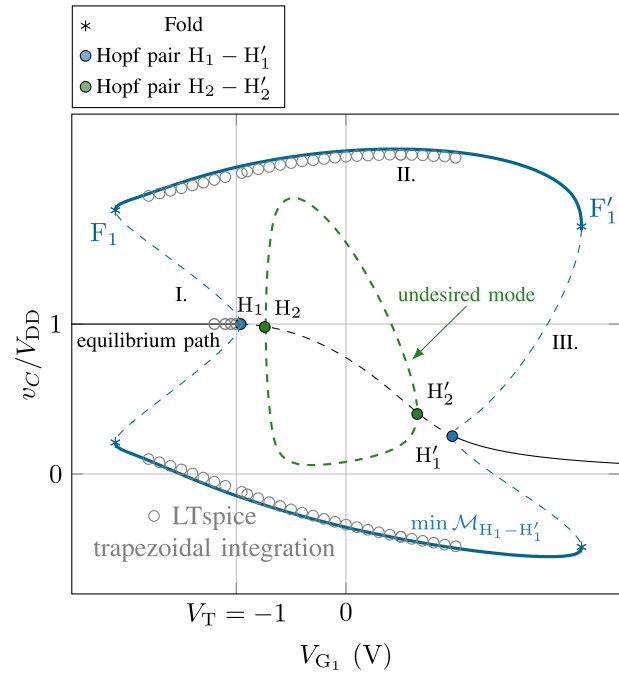


Fig. 6. Bifurcation diagram of the first active section with  $R_L = 1 \Omega$  per inductor in the artificial TL (dashed and solid lines correspond to the unstable and stable invariant sets, respectively). Equilibrium path and maxima and minima of the limit cycles in terms of the state variable  $v_C$  are represented.

#### A. First Active Stage

We will start with the simplest case, in which the first stage is the only active one in the oscillator (the other two stages are switched off). For the first active stage, the expected mode is  $\Omega_n^{(1,1)}$  as discussed in Section II. As can be seen from the schematics in Fig. 2, when only  $I_1$  is active (i.e.,  $I_2(x_{12}/C_6 + x_{14} < V_T, x_{16})$  and  $I_3(x_{20}/C_{10} + x_{22} < V_T, x_{24})$ ), the feedback structure, consisting of a single  $LC \pi$  network, is easily identified as a simple common source Colpitts oscillator with a single resonant tank. The rest of the network acts as a redundant load of the resonator and oscillator output. The distributed amplifier oscillator model possesses a single stable EP  $\mathbf{x}_0$  (EP) when  $V_{GS_i} \leq V_T, i = 1, 2, 3$ . Continuation of this EP versus  $V_{GS_1}$  provides an EP path (see Fig. 6) that is traced in terms of  $v_C/V_{DD}$  where  $v_C = x_8$  in the schematics of Fig. 2. This continuation reveals two pairs of Hopf bifurcations at which two periodic oscillation curves are generated and extinguished when increasing  $V_{GS_1}$  (see Fig. 6). The periodic solutions are traced in terms of the maximum  $\max_{v_C/V_{DD}} \Gamma(V_{GS_i})$  and minimum  $\min_{v_C/V_{DD}} \Gamma(V_{GS_i})$  of the waveform  $v_C/V_{DD}$ . In Fig. 6 and the rest of this manuscript, we follow the convention that solid lines correspond to stable invariant sets and dashed lines to unstable ones. The variation of the normalized frequency versus  $V_{G_1}$  is shown in Fig. 7. The normalized frequency of the periodic oscillation obtained between  $H_1$  and  $H_1'$  (oscillatory mode  $\Omega_n^{1,1} = 1$ , denoted as Osc. 1) corresponds to the desired operation. On the other hand, the periodic solution obtained between  $H_2$  and  $H_2'$  (mode denoted as Osc. 2) corresponds to an undesired low-frequency oscillation, coming from the bias circuitry. The variation of its normalized frequency versus  $V_{G_1}$  is also shown in Fig. 7,

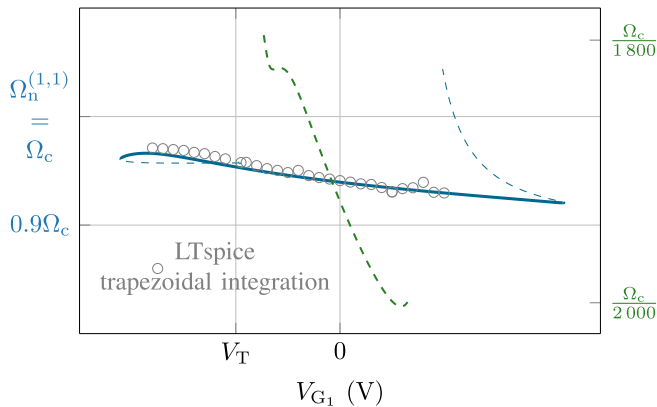


Fig. 7. Bifurcation diagram of the first active section with  $R_L = 1 \Omega$  per inductor in the artificial TL (dashed and solid lines correspond to the unstable and stable invariant sets, respectively). The normalized frequency of the desired mode is given in the left y-axis, whereas that of the undesired low-frequency oscillation is given in the right y-axis.

with values in the right axis. Bifurcation  $H_1$  leads to a stable oscillation after the fold bifurcation  $F_1$  in the periodic solution path. In contrast, the undesired low-frequency mode generated at  $H_2$  is unstable. To understand the stability properties of the two periodic paths, we will take into account the following Hopf bifurcation relationships (valid only in the neighborhood of the bifurcation) [12]:

$$\text{dc}^m \rightleftharpoons \text{dc}^{m+2} + P^m \quad \text{supercritical} \quad (15)$$

$$\text{dc}^m + P^{m+1} \rightleftharpoons \text{dc}^{m+2} \quad \text{subcritical} \quad (16)$$

where dc indicates a dc solution, and  $P$  indicates a periodic solution;  $m$  is the number of eigenvalues of the dc solution in the RHS and the number of Floquet multipliers of the periodic solution outside the unit circle. In the rightward sense (leftward sense), the relationships correspond to direct (inverse) Hopf bifurcations [12].

If a supercritical bifurcation occurs from a stable dc solution ( $m = 0$ ), the generated periodic oscillation curve will initially be stable. If a subcritical Hopf bifurcation occurs from a stable dc solution ( $m = 0$ ), the generated periodic oscillation curve will initially be unstable, with a real Floquet multiplier larger than 1. This is the case of bifurcation  $H_1$  in Fig. 6, which arises from a stable dc solution of the type  $\text{dc}^0$  and fulfills the relationship (16). However, this oscillatory solution passes through the fold bifurcation  $F_1$  in a periodic regime, where it becomes stable, as obtained through the analysis of the Floquet multipliers. In fact, the bifurcation relationship of a fold bifurcation in periodic regime is as follows:

$$\emptyset \rightleftharpoons P^m + P^{m+1} \quad (17)$$

where  $\emptyset$  indicates no solution.

The Hopf bifurcation pair  $H_1$  and  $H_1'$  is subcritical at the two points. On the other hand, the Hopf bifurcation pair  $H_2$  and  $H_2'$  is supercritical at the two points. Supercritical and subcritical bifurcations are generally easy to distinguish from the inspection of the solution curves. However, their distinction at the bifurcation point (without tracing the solution curves) requires the evaluation of a coefficient derived from

the normal form representation of the dynamical system [13]. This coefficient will be used in Section V to distinguish supercritical and subcritical bifurcations in a two-parameter plane.

At  $F_1$ , fulfilling (15) in a rightward sense with  $m = 1$ , the real multiplier (resulting from the subcritical Hopf bifurcation) enters the unit circle through the point  $(1, 0)$ . At the second fold bifurcation  $F_1'$  fulfilling (15) in a leftward sense with  $m = 1$ , a real multiplier escapes from the unit circle through  $(1, 0)$ . The subcritical nature of the Hopf pair  $(H_1, H_1')$ , together with the fold bifurcations  $(F_1, F_1')$ , gives rise to the hysteresis. This is because in the  $V_{G_1}$  intervals comprised between  $F_1$  and  $H_1$ , and between  $H_1'$  and  $F_1'$ , the stable oscillations coexist with stable dc solutions. In other words, if the circuit is energized enough, it is possible to sustain oscillations for control voltages below the threshold  $V_T$ . The detected hysteresis will be validated experimentally in Section IV-D.

As already indicated, the Hopf bifurcation pair  $(H_2, H_2')$  corresponds to an undesired low-frequency oscillation. Bifurcation  $H_2$  occurs from an unstable dc solution with  $m = 2$ , since this dc solution has the pair of eigenvalues  $\lambda_{i,i+1}$  associated with the oscillation mode Osc. 1 in the RHS. Note that the pair of complex-conjugate eigenvalues that cross at  $H_2$  is different, since they provide the oscillation mode Osc. 2. Because the low-frequency mode Osc. 2 arises from a dc solution of the type  $\text{dc}^2$ , the periodic solution generated at  $H_2$  will be initially unstable, according to (15). This is understood by considering that a small amplitude limit cycle (in the neighborhood of the bifurcation) cannot overcome the original instability of the dc solution, associated with the eigenvalues that give rise to Osc. 1. The analysis of the Floquet multipliers predicts the unstable behavior of the whole collection of periodic orbits comprised between  $H_2$  and  $H_2'$ , which exhibit a pair of complex-conjugate multipliers outside the unit circle. Therefore, this low-frequency oscillation will not be physically observable.

Fig. 8 shows the voltage waveforms (in terms of  $v_C/V_{DD}$ ) of the steady-state oscillation obtained for the control voltage  $V_{G_1} = 0 \text{ V}$ . The blue waveform, corresponding to mode Osc. 1 (with frequency  $\Omega_c = 1 \implies f_c = 127 \text{ Hz}$ ), is stable and, thus, observable in practice. On the other hand, the violet waveform, corresponding to mode Osc. 2 (with frequency  $f_c = 66 \text{ mHz}$ ) is unstable and, thus, reachable only from the null set of initial values. The stable waveform of mode Osc. 1 has been compared with the one obtained using independent simulations, incorporating LTspice (trapezoidal time-domain integration). The resulting steady-state waveform is shown in Fig. 8, where it has been traced with circles. The time shift, with respect to the one obtained through the steady-state analysis of Section III-A, is due to the autonomous nature of the solution.

The stable section of the oscillation curve of mode Osc. 1 has also been validated with independent simulations using LTspice (trapezoidal time-domain integration). The minima and maxima of the steady-state oscillation, when varying  $V_{G_1}$ , are represented with circles in Fig. 6. As can be seen, there is excellent agreement with the path obtained

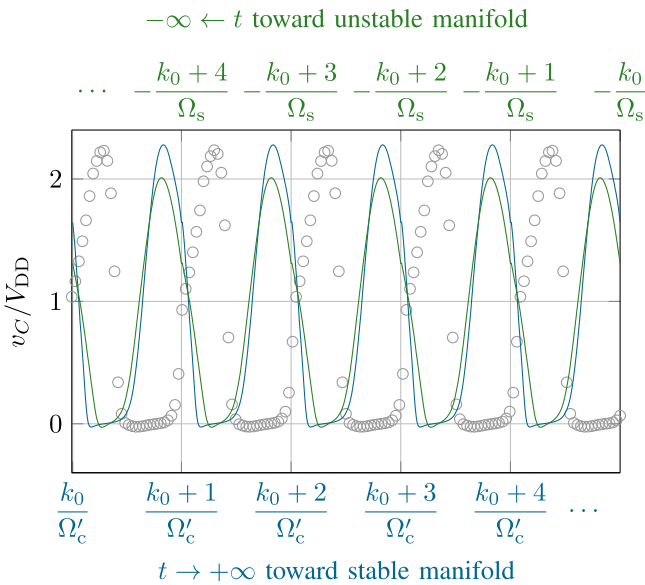


Fig. 8. Five periods of the steady-state periodic solution, corresponding to the mode Osc. 1, when only the first device is active at  $V_{G_1} = 0$  V in the time domain. The blue waveform associated with the bottom  $x$ -axis corresponds to a desired periodic solution of frequency  $\Omega'_c \doteq 0.94\Omega_c \doteq 119$  Hz, and the green trace associated with the top  $x$ -axis depicts the unstable low-frequency periodic solution  $\Omega_s \doteq 66$  mHz. Constant  $k_0 \in \mathbb{N}$  is the chosen fixed initial index of the steady-state period. The gray circles correspond to the steady-state solution obtained with LTspice trapezoidal integration.

through the method in Section III-A. Note that to obtain the oscillatory solution below the threshold voltage and confirm the existence of the fold bifurcation  $F_1$ , we need to carefully select a consistent initial condition [27] of the integration. The time-domain integration becomes complicated near the fold point  $F'_1$ , because the transient response takes an excessively long time to settle due to the low damping factor near the bifurcation.

We have seen that, except for the existence of an unstable parasitic variety of low-frequency oscillations, the first section of the oscillator does not cause any problems. Truly delicate complications are hidden in the remaining structure to which the same workflow scheme in this section will be applied.

### B. Second Active Stage

Now, we will switch off the first and third active devices. For the second active stage, the expected desired mode is  $\Omega_n^{(2,1)} = 1/2$ , according to (1). By continuation of EP, when varying control voltage  $V_{G_2}$ , a rich dynamic emerges, as seen in Fig. 9(a). In this case, three pairs of Hopf bifurcations and one sporadic Hopf point are detected in the EP path. When increasing  $V_{G_2}$  above the threshold voltage, the first Hopf bifurcation  $H_1$  gives rise to the onset of an oscillation at the frequency  $\Omega_n^{1,1} = \Omega_n^{2,2} = 1$  [Fig. 9(b)]. This frequency is common to that of the stable oscillation obtained when only the first stage was active. However, it is not the expected one when tuning  $V_{G_2}$ . It is undesired in this case because  $k = 2$  (see Section II). The two Hopf bifurcations  $H_1$  and  $H'_1$  are subcritical and fulfill (16) with  $dc^0$  in the left-hand side. The oscillation that arises at  $H_1$  is initially unstable, but, as predicted with the Floquet multipliers, it becomes

stable at the fold bifurcation  $F_1$ , which fulfills (17) with  $m = 1$ . However, at the period-doubling bifurcation PD, a multiplier escapes from the unit circle through  $(-1, 0)$ , and the oscillation becomes unstable again. This is a branching point from which a period-doubled solution emerges. Then, the sequence of fold points  $F_2 \rightarrow F_3 \rightarrow F_4$  occurs until the stable manifold of the desired mode  $\Omega_n^{(2,1)}$  is reached. Note that this is the mode expected when tuning  $V_{G_2}$ . This manifold at the desired frequency  $\Omega_n^{(2,1)} = 1/2f_c$  (shown in red) uniquely remains stable for a wide range of control voltage until the inverse subcritical sporadic Hopf point  $H_4$  is reached. This result will also be observed experimentally, as shown in Section IV-D.

Note that other manifolds of undesired oscillatory solutions arise from the remaining Hopf bifurcations. As seen in Section II, this is due to the multiresonant nature of the feedback structure, since the second active stage undergoes feedback through  $H_2(s)$  in Fig. 3. Also, note that the manifold arising from Hopf point  $H_2$  is not properly terminated in the inverse counterpart  $H'_2$ , because convergence of the numerical continuation becomes very difficult near the  $H'_1$  point. Additional oscillations arise from Hopf bifurcations of unstable dc solutions (due to the previous and subsequent generation of oscillatory solutions). To be more specific, in  $H_2$ , we have  $m = 2$ , and in  $H_3$ , we have  $m = 4$ , so according to the bifurcation relationships of (15) and (16), the generated oscillations are unstable in the neighborhood of the respective Hopf bifurcations. The analysis of the Floquet multipliers shows that they never stabilize.

The above results have been validated through the explicit integration scheme Runge–Kutta–Dormand–Prince 45, which is natively implemented in the MATLAB ODE suite. Note that only stable sections can be obtained through time integration. The results are represented with circles in Fig. 9(a). They correspond to the stable dc solution, the stable periodic oscillation at  $\Omega_n^{(2,2)}$  ( $f_c \doteq 127$  Hz), and the stable subharmonic oscillation at  $\Omega_n^{(2,1)}$  ( $f_c \doteq 63$  Hz). As can be seen, there is excellent agreement.

### C. Third Active Stage

Now, the first and second active devices are switched off, and we analyze the circuit under variations in the tuning voltage of the third stage. For the third active stage, the desired mode is  $\Omega_n^{(3,1)} = 1/4(\sqrt{5}-1) \doteq 0.31$  according to (1) and [2]. This investigation is crucial, because the small-signal analysis, both in [1] and in Section II, has shown that the buildup condition is (nontrivially) met at two frequencies. Thus, there is a question whether and under what conditions the desired mode will become stable. Now, the feedback is the most complicated, given by the passive function  $H_3(s)$  (see Fig. 3). As shown in Fig. 9(c), above the threshold voltage, there is a sequence of Hopf bifurcations from the EP that lie close together. In Fig. 9(c), they are distinguished using half-colored marks to highlight their order of appearance. The normalized frequency variation of the various modes versus  $V_{G_3}$  is shown in Fig. 9(d). This figure shows that, in this case, just one undesired mode corresponding to  $\Omega_n^{(3,2)} = 1/4(\sqrt{5}+1)$  is

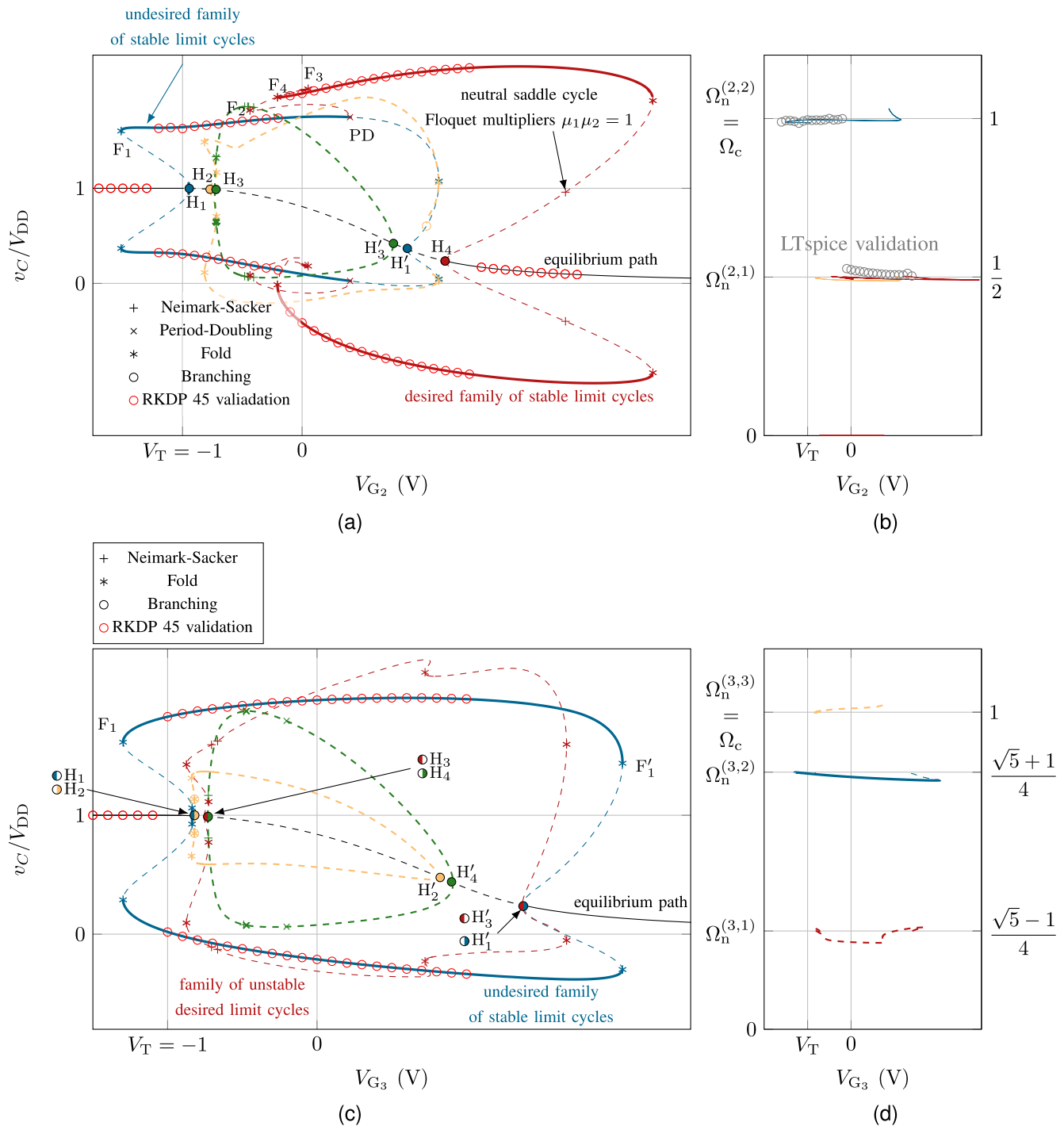


Fig. 9. Bifurcation diagram of the second and third stages with  $R_L = 1 \Omega$  per inductor in the artificial TL (dashed and solid lines correspond to the unstable and stable invariant sets, respectively). Equilibrium path and maxima and minima of the limit cycles in terms of the state variable  $v_C$  of (a) second and (c) third stages, and normalized frequency of the limit cycle families of (b) second and (d) third stages. Red marks are steady-state local maxima and minima obtained using explicit Runge–Kutta–Dormand–Prince 45 integration scheme.

stable, thus contradicting the small-signal assumption that the stable mode  $\Omega_n^{(i,k)}$  of the lowest  $k \in \mathbb{N}$  will be stable with nonzero losses [1]. Note that mode  $\Omega_n^{(3,2)} = 1/4(\sqrt{5} + 1)$  is generated from a stable dc solution in a subcritical bifurcation [dc<sup>0</sup> in the left-hand side of (16)]; it becomes stable after undergoing a fold bifurcation  $F_1$  (fulfilling (17) in a rightward sense with  $m = 1$ ), where a real and positive multiplier enters the unit circle. This mode is stable until reaching the

second fold bifurcation  $F'_1$  (fulfilling (17) in a leftward sense with  $m = 1$ ), where a real and positive multiplier escapes from the unit circle. All the other modes, generated at the Hopf bifurcations  $H_2$ ,  $H_3$ , and  $H_4$ , arise from unstable dc solutions and never stabilize. In  $H_2$ , we have  $m = 2$ ; in  $H_3$ , we have  $m = 4$ , and in  $H_4$ , we have  $m = 6$ , so according to bifurcation relationships (15) and (16), they are unstable in the neighborhood of the respective Hopf bifurcations. The analysis

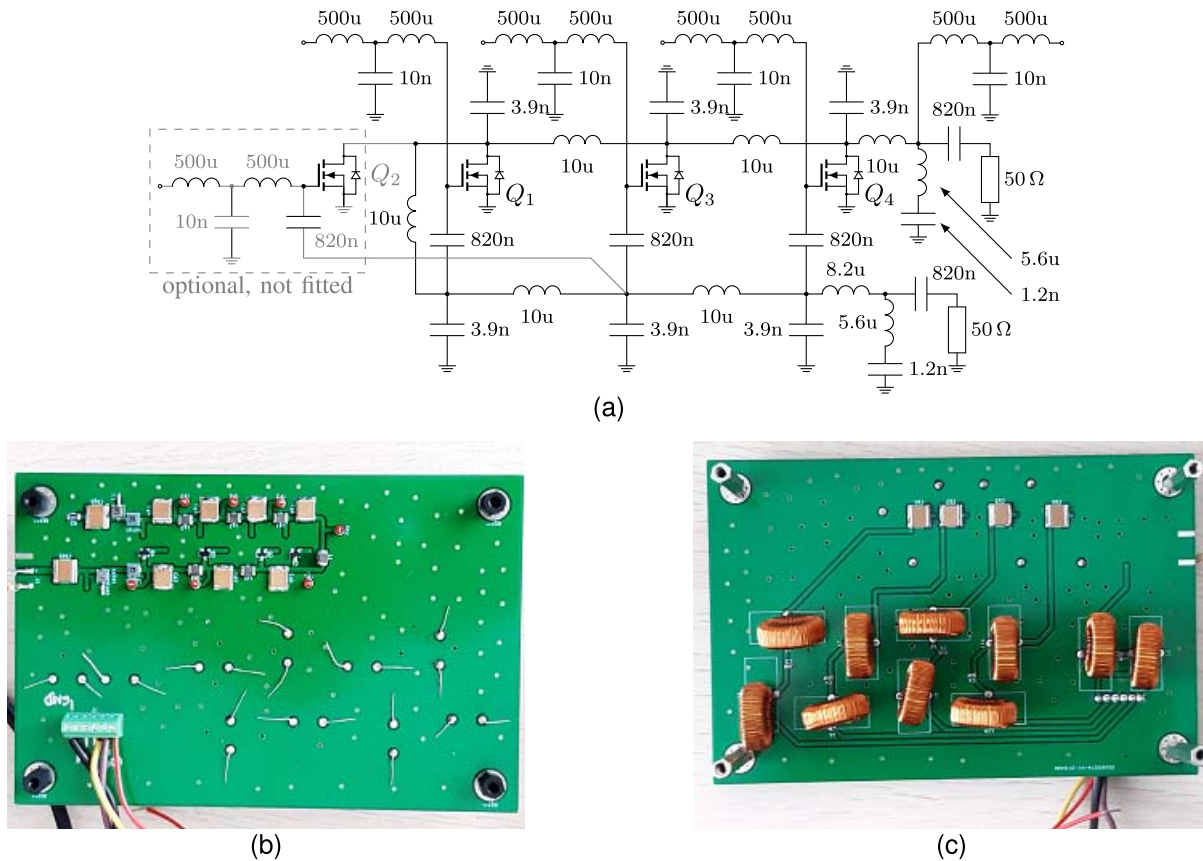


Fig. 10. Implementation of the distributed amplifier oscillator and implementation. (a) Detailed schematic. (b) Top view. (c) Bottom view with biasing circuitry. Optional cross-coupled FET investigated in [1] is not used.

of the Floquet multipliers shows that they never stabilize. The desired mode  $\Omega_n^{(3,1)}$  arises at the Hopf bifurcation  $H_3$  [see Fig. 9(c)] and is one of those modes that never stabilize.

The results have also been validated through the explicit integration scheme Runge–Kutta–Dormand–Prince 45. Note that only stable sections can be obtained through time integration. The results are represented with circles in Fig. 9(c). They correspond to the stable dc solution and the stable undesired periodic oscillation at  $\Omega_n^{(3,2)} = 1/4(\sqrt{5} + 1)$ . As can be seen, there is excellent agreement.

The possible stabilization of the desired mode  $\Omega_n^{(3,1)} = 1/4(\sqrt{5} - 1)$  by losses will be addressed in Section V.

#### D. Experimental Validation of the Stability Analysis

For the experimental validation of the detected phenomena, we built a sample of the distributed-amplifier oscillator. A detailed schematic of this experimental circuit is shown in Fig. 10. The circuit was implemented as a double-sided PCB on a standard FR-4. As an active device, we chose a standard N-channel FET BSS138 (Onsemi). For more details on the implementation and design method, see [2] and [3]. The cutoff frequency  $f_c$  of the manufactured prototype is  $f_c = 1/\pi\sqrt{LC} \doteq 1.61$  MHz, and the impedance of the artificial TL is  $Z = 50 \Omega$ . This low frequency was chosen to be able to measure at different points of the circuit without significantly affecting the measurement. With regard to the

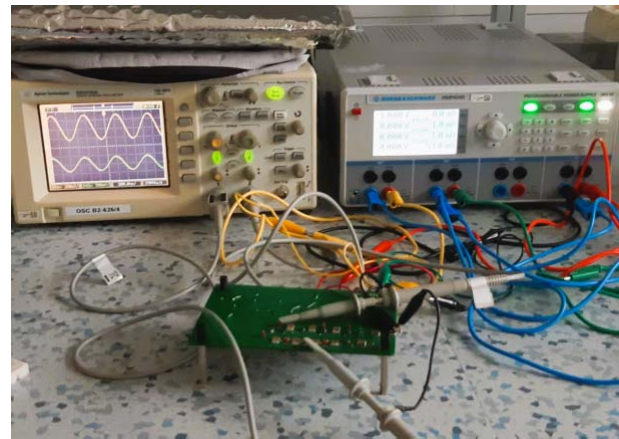


Fig. 11. Measurement setup: device under test (DUT), oscilloscope, and four-channel output power supply.

low-frequency realization, the measurement was carried out with a digital oscilloscope; see Fig. 11.

Considering the above values and using (1), the frequency of the desired mode when only the first stage is active should be  $f_c \doteq 1.61$  MHz. However, the nonlinear analysis in Section IV (Fig. 6) predicts the frequency  $0.95\Omega_c$ , which translates to  $f_{\text{first}} = 0.95 f_c \doteq 1.53$  MHz. This is in excellent agreement with the experimental measurement shown in the spectrum of Fig. 12. The frequency of the desired mode when only the

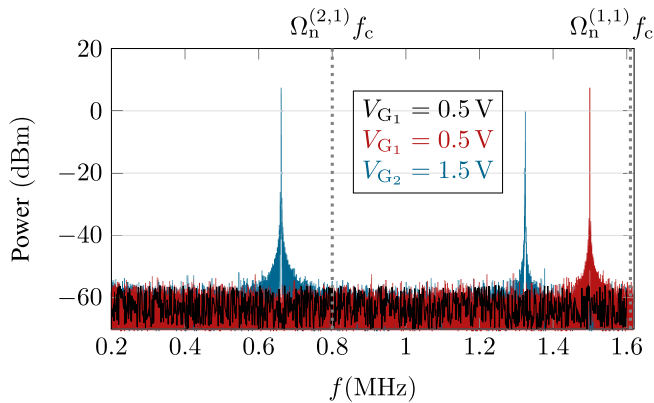


Fig. 12. In the experiment, the circuit first oscillates at the undesired mode  $\Omega_c$  (red spectrum); then, as the control voltage  $V_{G_2}$  is further increased, a period doubling occurs, which results in the desired mode  $\Omega_c/2$ . The upper horizontal axis shows the expected positions of the modes. Black and red spectra, both obtained for  $V_{G_2}$ , confirm the hysteresis phenomenon predicted in Fig. 9(a).

second stage is active should be  $\Omega_c/2$ . In the experiment, the circuit first oscillates at the undesired mode  $\Omega_c$  (red spectrum); then, as the control voltage  $V_{G_2}$  is further increased, a period doubling occurs, which results in the desired mode  $\Omega_c/2$ . This agrees with the predictions of Fig. 9(a), in which the second mode was obtained through a period doubling. The measured frequency of the second mode is  $f_{\text{second}} \doteq 650$  MHz, with a relative shift of 18%. This may seem like a significant difference, but, in fact, in the original paper [2], the measured frequency of the desired mode was  $0.42f_c$ . Our measured result is very close to this ratio at  $0.40f_c$  (Fig. 12). This shift can have a variety of causes, ranging from parasitic transistor capacities to phase prolongation of the feedback path due to layout design. Considering the accuracy of our model in the case of the first mode, we can conclude that this shift can be attributed to parasitic effects, which are accumulated in the oscillator implementation but are not present in the canonical model, thus indicating that they are parasitic.

The hysteresis predicted in the analysis of Section IV-A has also been found experimentally. First, we have increased the gate-bias voltage  $V_{G_1}$  from below threshold to  $V_{G_1} = 0.5$  V. The resulting spectrum at  $V_{G_1} = 0.5$  V is shown in black in Fig. 12. As one can see, there is no oscillation, so the dc solution is stable, in agreement with the predictions of Section IV-A. Then, we have decreased  $V_{G_1}$  from  $V_{G_1} = 1.6$  V (with the circuit in an oscillatory state) to the same value  $V_{G_1} = 0.5$  V. Now, for  $V_{G_1} = 0.5$  V, the circuit maintains the oscillation. The corresponding spectrum is shown in red in Fig. 12.

## V. SINGULARITIES OF CODIMENSION 2

As indicated in Section II, the distributed amplifier oscillator is intended to be a wideband VCO tuned by gate voltage pairs. In Section II, this was demonstrated using small-signal transconductance equivalents of the active devices plus a stability analysis based on the use of the system characteristic determinant  $\det \mathbf{Y}(s)$ . In Section IV, these results were refined using a nonlinear state-space model. We obtained the complete

solution curves and distinguished supercritical and subcritical bifurcations from the analysis of the solution curves. Here, we will consider the variation of two tuning parameters, as done in Section II and which will be included in parameter vector  $\mu$ . We will obtain the loci of Hopf bifurcations in the plane defined by these two parameters.

As we are not tracing the solution curves, we will distinguish supercritical and subcritical bifurcations using the normal form [15] from an analysis of the bifurcation itself. In the last century, great efforts were made to systematize the theory of normal forms of vector fields, and this successfully resulted into the well-established branch of dynamical system theory [14], [15].

Here, we limit ourselves to an equilibrium normal form only. Equation (3) is expanded around an EP into the truncated power series  $\dot{\mathbf{x}} = \mathbf{A}\mathbf{x} + a_1(\mathbf{x}) + a_2(\mathbf{x}) + \dots$ , where  $\mathbf{A}$  is assumed to be in Jordan canonical form. A coordinate change  $\mathbf{x} \mapsto \mathbf{y}$  is then performed to obtain a more advantageous form of less complexity than the original system [15]. The normal form of the Hopf bifurcation is usually given as follows [13]:

$$\dot{\mathbf{y}} = j\Omega_0\mathbf{y} + b_1\mathbf{y}|\mathbf{y}|^2 + \dots, \quad b_i \in \mathbb{C} \quad (18)$$

where  $\text{Re } b_1 := l_1$  is the first Lyapunov coefficient, and  $\mathbf{y}$  is a complex representation of the incipient oscillation in magnitude and phase as  $\mathbf{y} = A e^{j\Omega t}$ , where  $A$  is the amplitude, and  $\Omega$  is the frequency.

At this point, without losing clarity, it is enough to say that the generated periodic orbit is stable, and the Hopf bifurcation is supercritical if the first Lyapunov coefficient is negative,  $l_1 < 0$ . If this coefficient is positive  $l_1 > 0$ , the generated periodic orbit is unstable, and the Hopf bifurcation is subcritical.

In this section, the Hopf loci refer to the curves of Hopf points  $\mathcal{H}(\mu)$ , where  $\mu \in \mathbb{R}_p^2$  in the vector of the two parameters. As already stated, in a first analysis, this vector is  $\mu = (V_{G_2}, V_{G_3})$ . Fig. 13 presents the Hopf loci obtained under the variation of  $V_{G_2}$  and  $V_{G_3}$ , represented in the plane defined by these two parameters. There are four dominant distinct loci, corresponding to the various distinct modes detected in Section IV. To illustrate the frequencies of the oscillations generated/extinguished at the distinct loci, at points denoted with diamonds, we provide the eigenvalues  $\lambda_i$  causing the singularity of the EP linearization  $D\Phi(\mu)|_{\mathbf{x}_0}$  discussed in Section III-B. The normalized value of the frequency of  $\lambda = \pm 2\pi j 94$  Hz is  $\Omega = 94/127 \doteq 0.74$ , which corresponds the undesired mode  $\Omega_n^{(3,2)}$ . Note that such notation for the modes is only applicable when only one of the devices is active, that is, when moving along the axes of Fig. 13(a). On the  $V_{G_2}$  axis and the  $V_{G_3}$  axis are shown the Hopf bifurcations found in Sections IV-B and IV-C, respectively, in their respective colors used in Fig. 9. However, the eigenvalues in Fig. 13(a) evolve continuously from the modes analyzed in Sections II and IV.

The Hopf bifurcation loci of Fig. 13(a) provide very useful information on the oscillator tunability. One should consider that in an ideal distributed oscillator, we would have a single Hopf locus in the plane defined by each pair of tuning voltages, unlike what happens in Fig. 13(a). When the second and

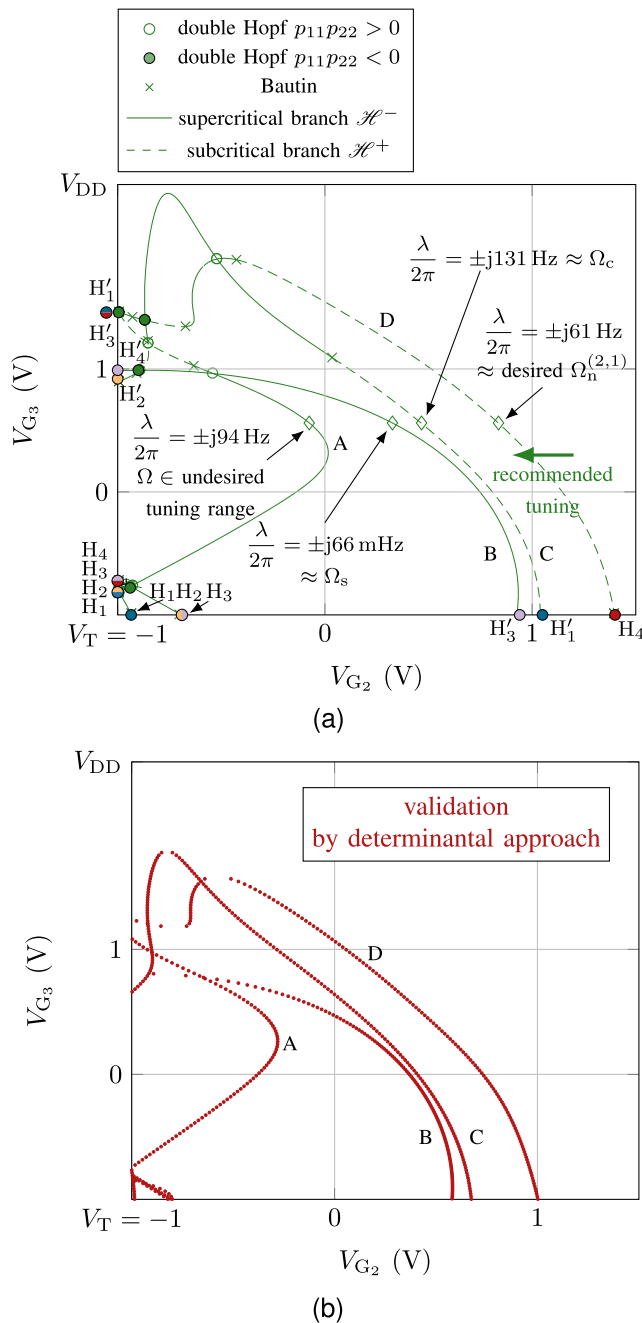


Fig. 13. Hopf loci when tuning the second and third transistor at  $R_L = 1 \Omega$ . (a) Through time-domain continuation. At points on the branches denoted with diamond marks, we give an example of eigenvalues  $\lambda$  causing singularity of the EP linearization  $D\Phi(\mu)|_{x_0}$ . These eigenvalues are linked to the modes introduced in Sections II and IV. On the  $V_{G_2}$  axis and  $V_{G_3}$  axis are shown the Hopf bifurcations found in Sections IV-B and IV-C, respectively, in their respective colors used in Fig. 9. Crossings of the loci are double-Hopf singularities. They are further classified according to normal form coefficients of which the most important is the unavoidable presence of *complicated* case  $p_{11}p_{22} < 0$  in the tuning region. (b) Through the calculation of the roots of the characteristic determinant. Note the excellent agreement.

third transistors are active, the Hopf locus corresponding to the desired mode is the rightmost one (locus D). In fact, the bifurcations shown in the horizontal axis (third transistor off) are those already analyzed in Fig. 9(a). When reducing  $V_{G_2}$  from above  $H_4$ , the desired mode ( $\Omega_n^{(2,1)}$ ) is generated at this subcritical bifurcation ( $H_4$ ) and becomes stable after a turning

point of the periodic solution curve. To the right of the locus D, the dc solution is stable. Then, when tuning the transistors from this dc-stable region to the left (see arrow), the oscillation generated corresponds to the desired mode and can be tuned through the variation of  $V_{G_2}$  and  $V_{G_3}$ , in various manners. Thus, it is recommended to start the tuning from the dc-stable region on the right. Fig. 13(a) also illustrates why we had a very bad behavior when only the third transistor was on [Fig. 9(c)]. The vertical axis of Fig. 13(a), which corresponds to this situation, is plagued with bifurcations, and the desired mode never stabilizes.

Our aim is also to provide practical tools for a prediction of the global-stability properties of the oscillator. Thus, we have implemented a method to obtain the Hopf loci making use of the characteristic determinant defined in Section II. Note that it is the determinant of a total admittance matrix that can be easily calculated in commercial software. We take into account that at a Hopf bifurcation, we have a pair of complex-conjugate zeroes crossing the imaginary axis. Consequently, we will replace  $s = \Sigma + j\Omega$  with  $j\Omega$ . Thus, at any Hopf bifurcation in terms of the parameter vector  $\mu$ , the following condition will be fulfilled:

$$\det \mathbf{Y}(\mu, j\Omega) = 0. \quad (19)$$

When splitting (19) into real and imaginary parts, one obtains a system of two equations in three unknowns, given by  $\Omega$  and the two components of the vector  $\mu$ , which will provide one or several curves in the plane defined by the two parameters in  $\mu$ . Note that because the frequency  $\Omega$  is autonomously generated, it will change through the Hopf locus, so it is an unknown of the complex equation. Equation (19) can be easily solved through a contour-intersection procedure [29]. In this method, we perform a triple sweep of the two components in  $\mu$  and  $\Omega$ . For each value of the first component  $\mu_1$ , we obtain (through an internal double sweep) the real and imaginary parts  $\text{Re}[\det \mathbf{Y}(\mu_2, j\Omega)]$  and  $\text{Im}[\det \mathbf{Y}(\mu_2, j\Omega)]$ . Next, we calculate the zero-value contours of these two surfaces, given by  $\text{Re}[\det \mathbf{Y}(\mu_2, j\Omega)] = 0$  and  $\text{Im}[\det \mathbf{Y}(\mu_2, j\Omega)] = 0$ . Then, all the Hopf loci points existing for the particular value  $\mu_1$  are obtained from the intersections of the two contours.

The results are presented in Fig. 13(b). As can be seen, there is some discrepancy. This is because the admittance matrix has been obtained with a commercial simulator where the transistor model is different. It is a Curtice model, instead of the model modification used in (4). The qualitative agreement is very good considering the dramatic difference between the two mathematical models. Recall the notes made in Section III on the piecewise smooth DAE used by commercial simulators and our smooth ODE model. This partial agreement between such different models proves that the obtained results are related to the circuit topology and not to transistor nonlinearity. We would also like to emphasize the excellent prediction capability of the contour-intersection method applied to the characteristic determinant (19). Moreover, in Fig. 13(a), a scaled version of the circuit is analyzed, whereas the circuit considered in Fig. 13(b) is not scaled. Once again, the agreement proves the robustness of the presented procedure.

The Hopf loci in Fig. 13(a) not only provide the parameter values at which the periodic modes are generated, but also very relevant information about the global circuit behavior. This is because some particular points of the loci have a significant impact on the circuit dynamics. They correspond to codimension 2 bifurcations, since they require the simultaneous fine-tuning of the two parameters in vector  $\mu$ . They are the Bautin and double-Hopf bifurcations, described next.

#### A. Bautin Bifurcation

We will denote  $\mathcal{H}^+(\mu)$  and  $\mathcal{H}^-(\mu)$  a section of the Hopf locus consisting of supercritical and subcritical Hopf bifurcations. Note that the superscript refers to the sign of the Lyapunov coefficient obtained from the normal form of the bifurcation. Then, from the continuity of the loci,  $\mathcal{H}(\mu) = \mathcal{H}^+(\mu) \cup \mathcal{H}^-(\mu) \cup \mathcal{B}(\mu)$ , where the values of  $\mathcal{B}(\mu)$  are generalized Hopf points at which  $l_1 = 0$ , known as Bautin bifurcations. Thus, the Hopf loci are divided into sections of subcritical and supercritical Hopf bifurcations and discrete transition points where  $l_1 = 0$ . This codimension 2 singularity will manifest itself as the collision of two limit cycles and a disappearance via a fold bifurcation of periodic orbits in the neighborhood [13]. When passing through a Bautin bifurcation, a subcritical Hopf bifurcation becomes supercritical or vice versa. Branches of subcritical and supercritical Hopf bifurcation points that may be encountered during the process of oscillator tuning are indicated in Fig. 13(a). This has been validated by comparing the predictions of Fig. 13 (for  $V_{G_2}$  below threshold and increasing  $V_{G_3}$ ) with the geometry of the Hopf bifurcations encountered in Fig. 9(c) versus  $V_{G_3}$ . There is an excellent agreement.

#### B. Double-Hopf Bifurcation

As gathered from Fig. 13(a), there can be intersections between two distinct Hopf loci, corresponding to double-Hopf bifurcations. These are points at which two distinct pairs of complex-conjugate eigenvalues of the EP cross the imaginary axis simultaneously. A more formal definition follows.

When two Hopf loci intersect,  $\mathcal{H}_1(\mu) \cap \mathcal{H}_2(\mu) = \widehat{\mathcal{H}}$  and the singular points  $\widehat{H} \in \widehat{\mathcal{H}}$  fulfill additional technical conditions on the generosity of the singularity given in [15], and we refer to  $\widehat{H}$  as a double-Hopf bifurcation. This has a 4-D normal form often written as follows [13], [15]:

$$\dot{y}_1 = y_1(\beta_1 + p_{11}(\beta)y_1^2 + p_{12}(\beta)y_2^2) \quad (20)$$

$$\dot{y}_2 = y_2(\beta_2 + p_{21}(\beta)y_1^2 + p_{22}(\beta)y_2^2) \quad (21)$$

where  $\beta_k$  and  $p_{ij}$  are appropriately selected, so that the resulting system is simpler; for details, see [13] and [15]. Under certain non-degeneracy conditions imposed on the normal form coefficients (see [13], [14]), up to 11 different unfolding scenarios are distinguished purely based on the  $p_{ij}$  coefficients. Their role is similar to that of the first Lyapunov coefficient in an ordinary Hopf bifurcation. Indeed, the Jordan canonical form associated with the linearization about the

double-Hopf bifurcation point is

$$\begin{bmatrix} 0 & -\omega_1 & | & 0 \\ \omega_1 & 0 & | & 0 \\ \hline 0 & -\omega_2 & | & 0 \\ \omega_2 & 0 & | & 0 \end{bmatrix}$$

where two distinct nonzero eigenvalues  $j\omega_1$  and  $j\omega_2$  must satisfy additional non-degeneracy conditions [14] as per usual.

In practice, the presence of a double-Hopf point will lead to different phenomena depending on the signs of the coefficients  $p_{ij}$ . From the various possibilities, we are interested only in the following.

- 1)  $p_{11}p_{22} > 0$  (*Simple Case*): An invariant 2-D torus  $\mathbb{T}^2$  is generated (quasi-periodic solution). In the experiment, this gives rise to a densely filled quasi-periodic invariant torus.
- 2)  $p_{11}p_{22} < 0$  (*Complicated Case*): A tri-torus  $\mathbb{T}^3$  breakdown occurs via heteroclinic connection; thus, a local birth of chaos will take place. This scenario of chaos formation often gives rise to a spectrum with an abnormally high level of noise. From a practical point of view, we want to avoid such singularities.

In Fig. 13(a), we followed Kuznetsov's notation  $p_{ij}p_{ij}$ ,  $i, j = 1, 2$ , of normal forms [13]. In the parametric plane of the two tuning voltages  $V_{G_2}$  and  $V_{G_3}$ , we have four double-Hopf bifurcations fulfilling  $p_{11}p_{22} < 0$ . Thus, they are associated with *complicated* cases. The presence of these points indicates that during the process of tuning, the chaotic nature of the system will inevitably manifest. This has been encountered in the experiment as well. In fact, both the quasi-periodic and chaotic behaviors predicted by the loci in Fig. 13 have been observed in the experimental measurements. Fig. 14(a) shows a quasi-periodic trajectory, while Fig. 14(b) shows a chaotic attractor. The corresponding spectra are shown (in different colors) in Fig. 14(c).

We would like to emphasize that this analysis of double-Hopf bifurcations provides, for the first time to our knowledge, a rigorous mathematical justification of the chaotic spectra often found experimentally in multidevice oscillators and other circuits.

## VI. POSSIBLE STABILIZATION OF THE OSCILLATOR

In this section, we will deal with the crucial question on the possible mode stabilization through the effect of losses as stated by Škvor et al. [1], Divina and Škvor [2], and Acampora and Georgiadis [8]. First, we will discuss the procedure to eliminate the low-frequency oscillations due to the bias circuitry. Then, we will address the undesired higher frequency modes resulting from the impact of the feedback paths, illustrated in Figs. 1 and 3.

#### A. Suppression of Oscillations Due to the Bias Circuitry

Even though all the low-frequency modes detected in our investigation were unstable, it can be convenient to suppress them in order to minimize the risk of interference with the desired modes, and the subsequent onset of undesired phenomena through a collision process [15], for instance.

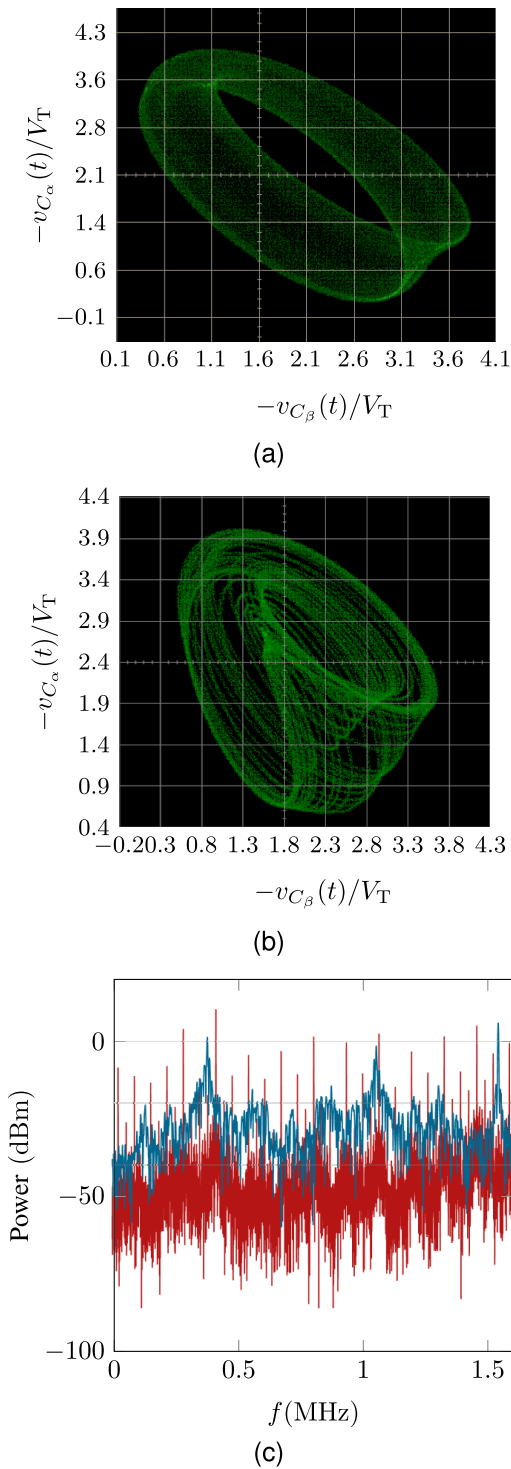


Fig. 14. Measured undesired phenomena. (a) Quasi-periodicity. (b) Chaotic invariant set. Measured voltages correspond to the state variables in the schematics of Fig. 2 denoted as  $v_{C_\alpha} = x_6$  and  $v_{C_\beta} = x_8$ . (c) Measured spectrum of the quasi-periodic regime is shown in red, and spectrum of the chaotic attractor is shown in blue.

To suppress these modes in an efficient manner, we will make use of the Hopf bifurcation loci that were described in Section V. However, instead of using two tuning voltages as parameters, we will use one tuning voltage and a stabilization series resistor  $R_{V_i}$ ,  $i = 1, 2, 3$  (see the schematic in Fig. 2).

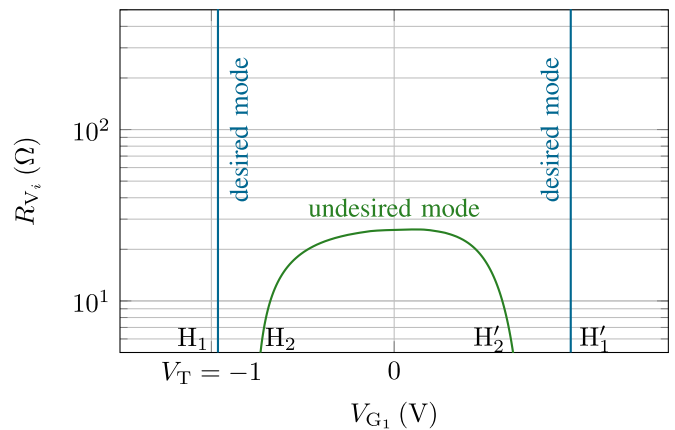


Fig. 15. Suppression of the undesired low-frequency oscillation. Hopf bifurcation loci in the plane defined by  $V_{G_2}$  and  $R_{V_i}$  (see schematic of Fig. 2). Undesired oscillation occurs inside the locus in green.

Note that the procedure can be repeated in a whole interval of the other tuning voltage (the one that is kept constant for each loci calculation). Fig. 15 presents the loci obtained when only the first stage is active, traced in the plane defined by  $V_{G_1}$  and  $R_{V_1}$ . This is sufficient, because, as shown in Sections IV-B and IV-C, the undesired low-frequency mode is present and unchanged in all the three stages when only a single device is active. In Fig. 15, two distinct loci can be observed, one corresponding to the desired mode and the other corresponding to the undesired low-frequency oscillation. Note that we have used the same color coding as in the rest of this article. The two oscillations occur inside the boundaries of the respective loci. The desired mode is not affected by the changes in  $R_{V_1}$  (it remains constant along the  $R_{V_1}$  axis). However, the undesired low-frequency oscillation vanishes for values of the series resistance above  $R_{V_1} = 26 \Omega$ . Thus, by just increasing this resistance, one will suppress the low-frequency mode.

### B. Suppression of Higher Frequency Modes

The analyses and measurements of Sections IV and V demonstrated quasi-periodic and chaotic behaviors of the distributed amplifier oscillator that are completely unacceptable. As shown here, these phenomena are present in the oscillator up to at least  $R_L = 1 \Omega$  per inductor in the artificial TL. Hence, we will investigate if it is possible to avoid these phenomena considering higher losses in the system. This, in fact, is the assumption followed by all relevant works on the distributed amplifier oscillator [2], [3], [8], [9]. In this section, we show that this is not completely true. With this aim, we will carry out an analysis through bifurcation loci analogous to the one described in the previous subsection. Fig. 16(a) presents the Hopf loci calculated in the plane defined by  $V_{G_3}$  and  $R_L/Z$ , thus denoted as  $\mathcal{H}(V_{G_3}, R_L/Z)$ . The aim is to investigate the possible stabilization effect of  $R_L$  as suggested in previous works [2], [3], [8], [9].

In Fig. 16(a), we can distinguish several loci that correspond to the modes obtained in the analysis of the third active stage in Section IV-C. The frequency of the mode corresponding to each locus is indicated. For  $R_L = 1$ , the Hopf bifurcations

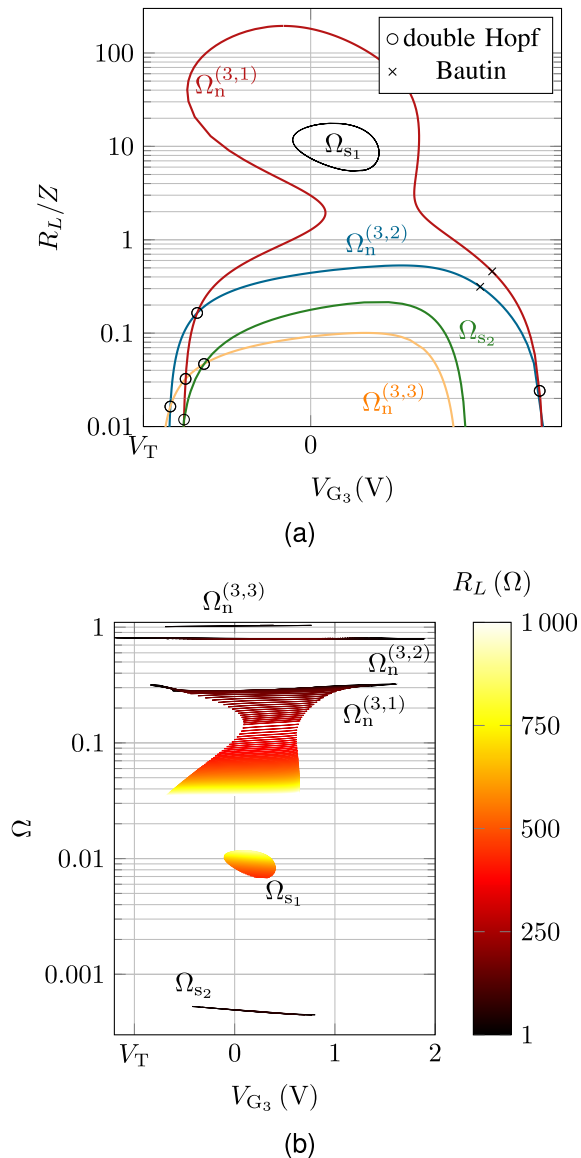


Fig. 16. Two-parametric bifurcation diagram of the third stage. (a) Hopf loci when losses  $R_L$  are considered. (b) Corresponding frequencies of the limit cycles  $\Gamma(V_{G_3})$  for given losses  $R_L$ .

agree with those detected in Fig. 9(c). The Hopf locus  $\Omega_{s_2}$  corresponds to the undesired low-frequency mode investigated in Section VI-A. As can be seen, for low  $R_L$ , there are plenty of modes. When increasing  $R_L$ , the Hopf points, in terms of  $V_{G_3}$ , approach their inverse Hopf pair counterpart until they disappear. With a large portion of losses  $30 \Omega < R_L < 200 \Omega$ , the desired mode  $\Omega_n^{(3,1)}$  is the only remaining one. For even greater losses, the closed Hopf locus  $\Omega_{s_1}$  (traced in black) appears, which is caused by wave reflection due to mismatch in the artificial TL.

Even though, as gathered from Fig. 16(a), the unique mode has been achieved under the original assumptions in [2], it is observed that the following hold: 1) the resulting limit-cycle paths at given losses tend to dramatically decrease in frequency as losses increase, as shown in Fig. 16(b) and 2) the oscillation amplitude becomes negligibly small.

To predict the impact on the steady-state oscillation frequency [Fig. 16(b)] and amplitude, we first found all the Hopf

points of an equilibrium for a fixed value of  $R_L$ , and then, their corresponding limit cycle manifolds were computed. This is the same workflow applied in Section IV. For each limit cycle of the manifold, its frequency  $1/T$  was found as in Fig. 7, for instance. This was repeated for  $R_L$  up to 1 k $\Omega$ . The resulting steady-state oscillation frequencies are shown with the color bar in Fig. 16(b). Note that the modeling of losses using  $R_L$  actually means a substantial change in the impedance of the artificial TL and, therefore, a significant mismatch at both ends. The presence of reflections in the TL degrades the performance of the oscillator and gives rise to the additional oscillation  $\Omega_{s_1}$  in Fig. 16(b).

### C. Design Strategy

Despite the potentiality of time-domain continuation for the investigation of nonlinear dynamics, the applicability of this method is limited to circuits that can be described with a set of nonlinear differential equations in state form. For a practical design, stability and bifurcation analysis tools compatible with the commonly used harmonic-balance software should be used; this will allow considering a full description of the circuit with arbitrary models and parasitic effects. As shown through the manuscript, those practical methods rely on the calculation of the total admittance matrix of the complete oscillator topology, defined at the device terminals. The proposed methods can also be of use for other multidevice configurations. Then, the procedure to obtain a reliable behavior would consist of the following stages.

- 1) Obtain the bias voltages of the active devices required for the oscillator tuning that should enable the desired frequency interval. This should be done according to the expressions (or procedure) given in [2], [3], [8], and [9]. This is the standard method used in most works.
- 2) Perform a small-signal stability analysis versus the tuning voltages through the pole-zero identification [28] of the determinant of the total admittance matrix, defined at the device nodes [see (2)], agreeing with the circuit characteristic determinant. This matrix is easily calculated in commercial harmonic-balance software. This initial stability analysis would warn about possible instabilities occurring when varying the tuning voltages. See the analysis of Fig. 5 as an example.
- 3) Evaluation of the impact of the instability in a global manner, making use of the Hopf bifurcation condition expressed in terms of the characteristic determinant, given by (19). Instead of an identification, we now perform a root calculation in terms of the real frequency  $\omega$  and two tuning parameters. The resulting bifurcation curves will provide the boundaries of existence of each oscillation mode [see Fig. 13(b)]. The root calculation is carried out through a contour intersection procedure [29].
- 4) To limit the impact of instability, resistors can be introduced at proper locations. Their values can be obtained making use of mode-boundary contours through the same root calculation of the characteristic determinant (in terms of the real frequency  $\omega$ ).

## VII. CONCLUSION

The purpose of this work was to carry out an as-thorough-as possible stability analysis of the distributed amplifier oscillator. Using a bifurcation theory toolkit, we have verified that mode jumps during oscillator tuning are a feature of the oscillator itself and are not caused by implementation issues and active device imperfections. This is especially frustrating for the designer, as the oscillator behaves as expected in some tuning voltage ranges from the small-signal analysis. For other values, bifurcations appear, which have, to date, been misinterpreted as implementation imperfections. We have also confirmed that it is possible to achieve uniqueness of oscillatory solution but at the cost of low oscillator efficiency and negligible amplitude. We hope that with this work, we conclude the possible future efforts in the realization of this distributed amplifier oscillator topology, and the research activities will stretch toward the synthesis of a multiloop feedback system with an unambiguous buildup condition.

APPENDIX  
STATE SPACE EQUATIONS

Parameters of the circuit in Fig. 2 are as follows:  $m = 0.6$ ,  $V_T = -1$  V,  $L_1 = L_2 = L_6 = L_7 = L_{10} = L_{11} = L_{14} = L_{15} = 40$  H,  $L_3 = L_5 = L_8 = L_9 = 125$  mH,  $L_{12} = L_{13} = (1/2 + m/2)125$  mH,  $L_{16} = L_{17} = 125(1 - m^2)/(2m)$  mH,  $V_{DD} = 2.5$  V,  $R_{V_1} = R_{V_2} = R_{V_3} = R_{V_{DD}} = 5$   $\Omega$ ,  $R_1 = R_2 = 50$   $\Omega$ ,  $C_1 = C_2 = C_5 = C_6 = C_9 = C_{10} = C_{13} = C_{15} = C_{17} = 10$  mF,  $C_3 = C_4 = C_7 = C_8 = C_{11} = C_{12} = 50$   $\mu$ F, and  $C_{14} = C_{16} = 25m$   $\mu$ F. Note that in the equations below, conductance terms ( $1/R_{C_i}$ ) are also included in parallel with shunt capacitors in artificial TL; however, since we consider them as 1  $\mu$ S, they are not shown in the schematics for clarity

$$\dot{x}_1 = \frac{1}{L_1}(V_{G_1} - x_1 R_{V_1} - x_2) \quad (22)$$

$$\dot{x}_2 = \frac{1}{C_1}(x_1 - x_3) \quad (23)$$

$$\dot{x}_3 = \frac{1}{L_2}\left(x_2 - \left(\frac{x_4}{C_2} + x_6\right)\right) \quad (24)$$

$$\dot{x}_4 = x_3 - i_{D_1}\left(\frac{x_4}{C_2} + x_6\right) \quad (25)$$

$$\dot{x}_5 = \frac{1}{L_3}(x_8 - x_5 R_{L_3} - x_6) \quad (26)$$

$$\dot{x}_6 = \frac{1}{C_3}\left(x_5 - x_7 + \left(x_3 - i_{D_1}\left(\frac{x_4}{C_2} + x_6\right)\right) - \frac{x_6}{R_{C_3}}\right) \quad (27)$$

$$\dot{x}_7 = \frac{1}{L_4}(x_6 - x_{14} - x_7 R_{L_4}) \quad (28)$$

$$\dot{x}_8 = \frac{1}{C_4}\left(x_9 - x_5 - \frac{x_8}{R_{C_4}} - I_1\left(\frac{x_4}{C_2} + x_6, x_8\right)\right) \quad (29)$$

$$\dot{x}_9 = \frac{1}{L_5}(x_{16} - x_9 R_{L_5} - x_8) \quad (30)$$

$$\dot{x}_{10} = \frac{1}{C_5}(x_{11} - x_{13}) \quad (31)$$

$$\dot{x}_{11} = \frac{1}{L_6}(V_{G_2} - x_{11} R_{V_2} - x_{10}) \quad (32)$$

$$\dot{x}_{12} = x_{13} - i_{D_2}\left(\frac{x_{12}}{C_6} + x_{14}\right) \quad (33)$$

$$\dot{x}_{13} = \frac{1}{L_7}\left(x_{10} - \left(\frac{x_{12}}{C_6} + x_{14}\right)\right) \quad (34)$$

$$\dot{x}_{14} = \frac{1}{C_7}\left(x_7 - x_{15} + \left(x_{13} - i_{D_2}\left(\frac{x_{12}}{C_6} + x_{14}\right)\right) - \frac{x_{14}}{R_{C_7}}\right) \quad (35)$$

$$\dot{x}_{15} = \frac{1}{L_8}(x_{14} - x_{22} - x_{15} R_{L_8}) \quad (36)$$

$$\dot{x}_{16} = \frac{1}{C_8}\left(x_{17} - \frac{x_{16}}{R_{C_8}} - x_9 - I_2\left(\frac{x_{12}}{C_6} + x_{14}, x_{16}\right)\right) \quad (37)$$

$$\dot{x}_{17} = \frac{1}{L_9}(x_{24} - x_{17} R_{L_9} - x_{16}) \quad (38)$$

$$\dot{x}_{18} = \frac{1}{C_9}(x_{19} - x_{21}) \quad (39)$$

$$\dot{x}_{19} = \frac{1}{L_{10}}(V_{G_3} - x_{19} R_{U_3} - x_{18}) \quad (40)$$

$$\dot{x}_{20} = x_{21} - i_{D_3}\left(\frac{x_{20}}{C_{10}} + x_{22}\right) \quad (41)$$

$$\dot{x}_{21} = \frac{1}{L_{11}}\left(x_{18} - \left(\frac{x_{20}}{C_{10}} + x_{22}\right)\right) \quad (42)$$

$$\dot{x}_{22} = \frac{1}{C_{11}}\left(x_{15} - x_{23} - \frac{x_{22}}{R_{C_{11}}} + \left(x_{21} - i_{D_3}\left(\frac{x_{20}}{C_{10}} + x_{22}\right)\right)\right) \quad (43)$$

$$\dot{x}_{23} = \frac{1}{L_{12}}\left(x_{22} - \left(\frac{x_{34}}{C_{17}} + (x_{23} - x_{33})R_2\right) - x_{23} R_{L_{12}}\right) \quad (44)$$

$$\dot{x}_{24} = \frac{1}{C_{12}}\left(-x_{29} - x_{25} - x_{17} - \frac{x_{24}}{R_{C_{12}}} - I_3\left(\frac{x_{20}}{C_{10}} + x_{22}, x_{24}\right)\right) \quad (45)$$

$$\dot{x}_{25} = \frac{1}{L_{12}}\left(x_{24} - \left(\frac{x_{30}}{C_{15}} + (x_{25} - x_{31})R_1\right) - x_{25} R_{L_{13}}\right) \quad (46)$$

$$\dot{x}_{26} = x_{29} - x_{27} \quad (47)$$

$$\dot{x}_{27} = \frac{1}{L_{14}}\left(\frac{x_{26}}{C_{13}} - x_{27} R_{V_{DD}} - V_{DD}\right) \quad (48)$$

$$\dot{x}_{28} = x_{31} \quad (49)$$

$$\dot{x}_{29} = \frac{1}{L_{15}}\left(x_{24} - \frac{x_{26}}{C_{13}}\right) \quad (50)$$

$$\dot{x}_{30} = x_{25} - x_{31} \quad (51)$$

$$\dot{x}_{31} = \frac{1}{L_{16}}\left(\frac{x_{30}}{C_{15}} + (x_{25} - x_{31})R_2 - \frac{x_{28}}{C_{14}}\right) \quad (52)$$

$$\dot{x}_{32} = x_{33} \quad (53)$$

$$\dot{x}_{33} = \frac{1}{L_{17}}\left(\frac{x_{34}}{C_{17}} + (x_{23} - x_{33})R_2 - \frac{x_{32}}{C_{16}}\right) \quad (54)$$

$$\dot{x}_{34} = x_{23} - x_{33}. \quad (55)$$

## ACKNOWLEDGMENT

The authors would like to thank Franco Ramírez (University of Cantabria, Santander, Spain) for his careful and patient assistance with a data preparation of the contour intersections method.

## REFERENCES

- [1] Z. Skvor, S. R. Saunders, and C. S. Aitchison, "Novel decade electronically tunable microwave oscillator based on the distributed amplifier," *Electron. Lett.*, vol. 28, no. 17, pp. 1647–1648, Aug. 1992.
- [2] L. Divina and Z. Skvor, "Experimental verification of a distributed amplifier oscillator," in *Proc. 25th Eur. Microw. Conf.*, Oct. 1995, pp. 1163–1167.
- [3] L. Divina and Z. Skvor, "The distributed oscillator at 4 GHz," *IEEE Trans. Microw. Theory Techn.*, vol. 46, no. 12, pp. 2240–2243, Dec. 1998.
- [4] N. Kumar and A. Grebennikov, *Broadband RF and Microwave Amplifiers*. Boca Raton, FL, USA: CRC Press, Jul. 2017.
- [5] T. T. Y. Wong, *Fundamentals of Distributed Amplification*. Norwood, MA, USA: Artech House, Sep. 1993.
- [6] N. Kumar and A. Grebennikov, *Distributed Power Amplifiers for RF and Microwave Communications*. Norwood, MA, USA: Artech House, Jun. 2015.
- [7] M. Ferran, *Artificial Transmission Lines for RF and Microwave Applications*. Hoboken, NJ, USA: Wiley, May 2015.
- [8] A. Acampora and A. Georgiadis, "Wideband voltage controlled oscillators for cognitive radio systems," in *Advances in Cognitive Radio Systems*. London, U.K.: InTech, Jul. 2012, pp. 1–24.
- [9] A. Collado, A. Acampora, and A. Georgiadis, "Nonlinear analysis and synthesis of distributed voltage controlled oscillators," *Int. J. Microw. Wireless Technol.*, vol. 2, no. 2, pp. 159–163, Apr. 2010.
- [10] S. T. Parker and L. O. Chua, *Practical Numerical Algorithms for Chaotic Systems*. Berlin, Germany: Springer, Jan. 1989.
- [11] V. Rizzoli and A. Neri, "State of the art and present trends in nonlinear microwave CAD techniques," *IEEE Trans. Microw. Theory Techn.*, vol. MTT-36, no. 2, pp. 343–356, Feb. 1988.
- [12] H. Kawakami, "Bifurcation of periodic responses in forced dynamic nonlinear circuits: Computation of bifurcation values of the system parameters," *IEEE Trans. Circuits Syst.*, vol. CS-31, no. 3, pp. 248–260, Mar. 1984.
- [13] Y. A. Kuznetsov, *Elements of Applied Bifurcation Theory*. Berlin, Germany: Springer, Jun. 2004.
- [14] S. Wiggins, *Introduction To Applied Nonlinear Dynamical Systems and Chaos*, 2nd ed. Berlin, Germany: Springer, Oct. 2003.
- [15] J. Guckenheimer and P. Holmes, *Nonlinear Oscillations, Dynamical Systems, and Bifurcations of Vector Fields*. Berlin, Germany: Springer, Feb. 1983.
- [16] B. D. O. Anderson and S. Vongpanitert, *Network Analysis and Synthesis: A Modern Systems Theory Approach*. Englewood Cliffs, NJ, USA: Prentice-Hall, 1973.
- [17] M. P. Kennedy, "Chaos in the Colpitts oscillator," *IEEE Trans. Circuits Syst. I, Fundam. Theory Appl.*, vol. 41, no. 11, pp. 771–774, Nov. 1994.
- [18] M. Bernardo, C. Budd, A. R. Champreys, and P. Kowalczyk, *Piecewise-smooth Dynamical Systems: Theory and Applications*. Berlin, Germany: Springer, Jan. 2008.
- [19] G. M. Maggio, M. Di Bernardo, and M. P. Kennedy, "Nonsmooth bifurcations in a piecewise-linear model of the Colpitts oscillator," *IEEE Trans. Circuits Syst. I, Fundam. Theory Appl.*, vol. 47, no. 8, pp. 1160–1177, Aug. 2000.
- [20] S. E. Sussman-Fort, S. Narasimhan, and K. Mayaram, "A complete GaAs MESFET computer model for SPICE (short papers)," *IEEE Trans. Microw. Theory Techn.*, vol. MTT-32, no. 4, pp. 471–473, Apr. 1984.
- [21] W. R. Curtice, "A MESFET model for use in the design of GaAs integrated circuits," *IEEE Trans. Microw. Theory Techn.*, vol. MTT-28, no. 5, pp. 448–456, May 1980.
- [22] W. R. Curtice, "GaAs MESFET modeling and nonlinear CAD," *IEEE Trans. Microw. Theory Techn.*, vol. MTT-36, no. 2, pp. 220–230, Feb. 1988.
- [23] H. Statz, P. Newman, I. W. Smith, R. A. Pucel, and H. A. Haus, "GaAs FET device and circuit simulation in SPICE," *IEEE Trans. Electron Devices*, vol. ED-34, no. 2, pp. 160–169, Feb. 1987.
- [24] E. L. Allgower and K. Georg, *Numerical Continuation Methods: An Introduction*. Berlin, Germany: Springer, Feb. 1990.
- [25] W. J. F. Govaerts, *Numerical Methods for Bifurcations of Dynamical Equilibria*. Philadelphia, PA, USA: Society for Industrial and Applied Mathematics, 2000.
- [26] A. Dhooge, W. Govaerts, Y. Kuznetsov, H. Meijer, and B. Sautois, "New features of the software matcont for bifurcation analysis of dynamical systems," *Math. Comput. Model. Dyn. Syst.*, vol. 14, no. 2, pp. 147–175, 2008.
- [27] P. Kunkel and V. Mehrmann, *Differential-Algebraic Equations: Analysis and Numerical Solution* (EMS Textbooks in Mathematics). Berlin, Germany: European Mathematical Society, Feb. 2006.
- [28] J. M. Collantes et al., "Pole-zero identification: Unveiling the critical dynamics of microwave circuits beyond stability analysis," *IEEE Microw. Mag.*, vol. 20, no. 7, pp. 36–54, Jul. 2019.
- [29] A. Suarez, S. Sancho, F. Ramirez, and M. Ponton, "Stability and oscillation analysis at circuit level and through semi-analytical formulations," *IEEE J. Microw.*, vol. 1, no. 3, pp. 763–776, Jul. 2021.

**Jan Filip** (Graduate Student Member, IEEE) received the M.Sc. degree in electrical engineering from Czech Technical University in Prague, Prague, Czech Republic, in 2020, where he is currently pursuing the Ph.D. degree in bifurcation theory and passive circuits synthesis.

Since 2019, he has been with Rohde & Schwarz, Vimperk, Czech Republic.

**Almudena Suárez** (Fellow, IEEE) was born in Santander, Spain. She received the Licentiate degree in electronic physics and the Ph.D. degree from the University of Cantabria, Santander, in 1987 and 1992, respectively, and the Ph.D. degree in electronics from the University of Limoges, Limoges, France, in 1993.

She is currently a Full Professor with the University of Cantabria and the Head of the Microwave Engineering and Radiocommunication Systems Research Group. She has authored the book *Analysis and Design of Autonomous Microwave Circuits* (IEEE-Wiley, 2009) and coauthored the book *Stability Analysis of Nonlinear Microwave Circuits* (Artech House, 2003).

Prof. Suárez was a member of the Board of Directors (BoD) of the European Microwave Association from 2012 to 2020, where she is the Publication Officer. She is a member of the Technical Committee of the IEEE International Microwave Symposium (IEEE MTT-S) and the European Microwave Week. She was the Chair of the 2014 and 2015 Editions of the IEEE Topical Conference on RF/Microwave Power Amplifiers (PAWR), Newport Beach and San Diego. She was the General Technical Program Committee (TPC) Chair of the European Microwave Week 2018. She was the Chair of the IEEE Microwave Magazine Best Paper Award Committee from 2017 to 2020. She was the Coordinator of the Communications and Electronic Technology Area for the Spanish National Evaluation and Foresight Agency (ANEP) from 2009 to 2013. She was an IEEE Distinguished Microwave Lecturer from 2006 to 2008. She was an Editor-in-Chief of the *International Journal of Microwave and Wireless Technologies* (Cambridge University Press journals) from 2013 to 2018. She is currently an Associate Editor of *IEEE Microwave Magazine* and the IEEE TRANSACTIONS ON MICROWAVE THEORY AND TECHNIQUES.

**Zbyněk Škvor** (Senior Member, IEEE) was born in Prague, Czech Republic, in 1961. He received the Ing. and Ph.D. degrees in radioelectronics from Czech Technical University in Prague (CTU), Prague, Czech Republic, in 1985 and 1994, respectively.

He was the Vice-Dean of CTU in 2001, where he was also the Dean in 2005. Since 1989, he has been with CTU, where he has been a Professor with the Department of Electromagnetic Field since 2002. Since 2015, he has been a Vice-Rector of CTU.

Dr. Škvor has been a Board of Directors (BoD) member of SEFI since 2017. He received the IEEE 2-nd Millennium Medal and Werner von Siemens prizes for research in 2002 and for scientific publication in 2004. He served as the Chapter/Section Chair and the Region 8 Voluntary Contribution Fund Coordinator. He was with the Radioengineering Society (Treasurer) from 1991 to 2019.